

The effect of plain-weaving on the mechanical properties of warp and weft *p*-phenylene terephthalamide (PPTA) fibers/yarns

M. Grujicic · R. Yavari · J. S. Snipes ·
S. Ramaswami · C.-F. Yen · B. A. Cheeseman

Received: 25 April 2014 / Accepted: 5 August 2014 / Published online: 15 August 2014
© Springer Science+Business Media New York 2014

Abstract Coarse-grained molecular statics/dynamics methods are first used to investigate degradation in the PPTA fiber/yarn tensile strength, as a result of the prior compressive or tensile loading. PPTA fibers/yarns experience this type of loading in the course of a plain-weaving process, the process which is used in the fabrication of ballistic fabric and flexible armor. The more common all-atom molecular simulations were not used to assess strength degradation for two reasons: (a) the size of the associated computational domain rendering reasonable run-times would be too small and (b) modeling of the mechanical response of multi-fibril PPTA fibers could not be carried out (again due to the limited size of the computational domain). However, all-atom simulations were used to (a) define the coarse-grained particles (referred to as “beads”) and (b) parameterize various components of the bead/bead force-field functions. In the second portion of the work, a simplified finite-element analysis of the plain-weaving process is carried out in order to assess the extent of tensile-strength degradation in warp and weft yarns during the weaving process. In this analysis, a new material model is used for the PPTA fibers/yarns. Specifically, PPTA is considered to be a linearly elastic, transversely isotropic material with degradable longitudinal-tensile strength and the longitudinal Young’s modulus. Equations governing damage and strength/stiffness

degradation in this material model are derived and parameterized using the coarse-grained simulation results. Lastly, the finite-element results are compared with their experimental counterparts, yielding a decent agreement.

Introduction

The present work deals with the damage induced into *p*-phenylene terephthalamide (PPTA) fibers/yarns during the plain-weaving process, the process which is used in the fabrication of flexible armor. Since the plain-weaving process is usually based on the use of two orthogonal families of yarns (generally referred to as warp, or end, and weft, fill or pick yarns), the work addresses differences in the mechanical history of the two yarn families and the role of these differences in the extent of damage sustained by the two yarn families. Consequently, the main topics overviewed in the remainder of this section include (a) the basics of plain-weaving; (b) degradation of weft and warp yarns during weaving; (c) PPTA high-performance fibers/yarns; and (d) prior experimental investigations of weaving-induced yarn damage.

The basics of plain-weaving

Figures 1a–d show the most common (plain, basket, satin, and triaxial) weaving patterns used in flexible-armor applications. Plain-weaving, Fig. 1a, is the subject of the present work. Plain-weaving is one of the key fabric-production technologies. It involves interlacing two families of yarns/fibers, in a predefined order, so as to form a fabric of the desired architecture and properties. Weaving is carried out using a machine called a loom. The warp yarns, which form the basic structure of the fabric and are aligned in the

M. Grujicic (✉) · R. Yavari · J. S. Snipes · S. Ramaswami
Department of Mechanical Engineering, Clemson University,
241 Engineering Innovation Building, Clemson, SC 29634-0921,
USA
e-mail: gmica@clemson.edu

C.-F. Yen · B. A. Cheeseman
Army Research Laboratory – Weapons & Materials Research
Directorate, Aberdeen Proving Ground, MD 21005-5069, USA

Report Documentation Page				Form Approved OMB No. 0704-0188	
Public reporting burden for the collection of information is estimated to average 1 hour per response, including the time for reviewing instructions, searching existing data sources, gathering and maintaining the data needed, and completing and reviewing the collection of information. Send comments regarding this burden estimate or any other aspect of this collection of information, including suggestions for reducing this burden, to Washington Headquarters Services, Directorate for Information Operations and Reports, 1215 Jefferson Davis Highway, Suite 1204, Arlington VA 22202-4302. Respondents should be aware that notwithstanding any other provision of law, no person shall be subject to a penalty for failing to comply with a collection of information if it does not display a currently valid OMB control number.					
1. REPORT DATE 15 AUG 2014		2. REPORT TYPE		3. DATES COVERED 00-00-2014 to 00-00-2014	
4. TITLE AND SUBTITLE The Effect of Plain-weaving on the Mechanical Properties of Warp and Weft p-phenylene Terephthalamide (PPTA) Fibers/yarns				5a. CONTRACT NUMBER	
				5b. GRANT NUMBER	
				5c. PROGRAM ELEMENT NUMBER	
6. AUTHOR(S)				5d. PROJECT NUMBER	
				5e. TASK NUMBER	
				5f. WORK UNIT NUMBER	
7. PERFORMING ORGANIZATION NAME(S) AND ADDRESS(ES) Clemson University,Department of Mechanical Engineering,241 Engineering Innovation Building,Clemson,SC,29634				8. PERFORMING ORGANIZATION REPORT NUMBER	
9. SPONSORING/MONITORING AGENCY NAME(S) AND ADDRESS(ES)				10. SPONSOR/MONITOR'S ACRONYM(S)	
				11. SPONSOR/MONITOR'S REPORT NUMBER(S)	
12. DISTRIBUTION/AVAILABILITY STATEMENT Approved for public release; distribution unlimited					
13. SUPPLEMENTARY NOTES					
14. ABSTRACT Coarse-grained molecular statics/dynamics methods are first used to investigate degradation in the PPTA fiber/yarn tensile strength, as a result of the prior compressive or tensile loading. PPTA fibers/yarns experience this type of loading in the course of a plain-weaving process, the process which is used in the fabrication of ballistic fabric and flexible armor. The more common allatom molecular simulations were not used to assess strength degradation for two reasons: (a) the size of the associated computational domain rendering reasonable run-times would be too small and (b) modeling of the mechanical response of multi-fibril PPTA fibers could not be carried out (again due to the limited size of the computational domain). However, all-atom simulations were used to (a) define the coarse-grained particles (referred to as ?????beads?????) and (b) parameterize various components of the bead/bead force-field functions. In the second portion of the work, a simplified finite-element analysis of the plain-weaving process is carried out in order to assess the extent of tensile-strength degradation in warp and weft yarns during the weaving process. In this analysis, a new material model is used for the PPTA fibers/yarns. Specifically, PPTA is considered to be a linearly elastic transversely isotropic material with degradable longitudinal- tensile strength and the longitudinal Young???'s modulus. Equations governing damage and strength/stiffness degradation in this material model are derived and parameterized using the coarse-grained simulation results. Lastly, the finite-element results are compared with their experimental counterparts, yielding a decent agreement.					
15. SUBJECT TERMS					
16. SECURITY CLASSIFICATION OF:			17. LIMITATION OF ABSTRACT Same as Report (SAR)	18. NUMBER OF PAGES 22	19a. NAME OF RESPONSIBLE PERSON
a. REPORT unclassified	b. ABSTRACT unclassified	c. THIS PAGE unclassified			

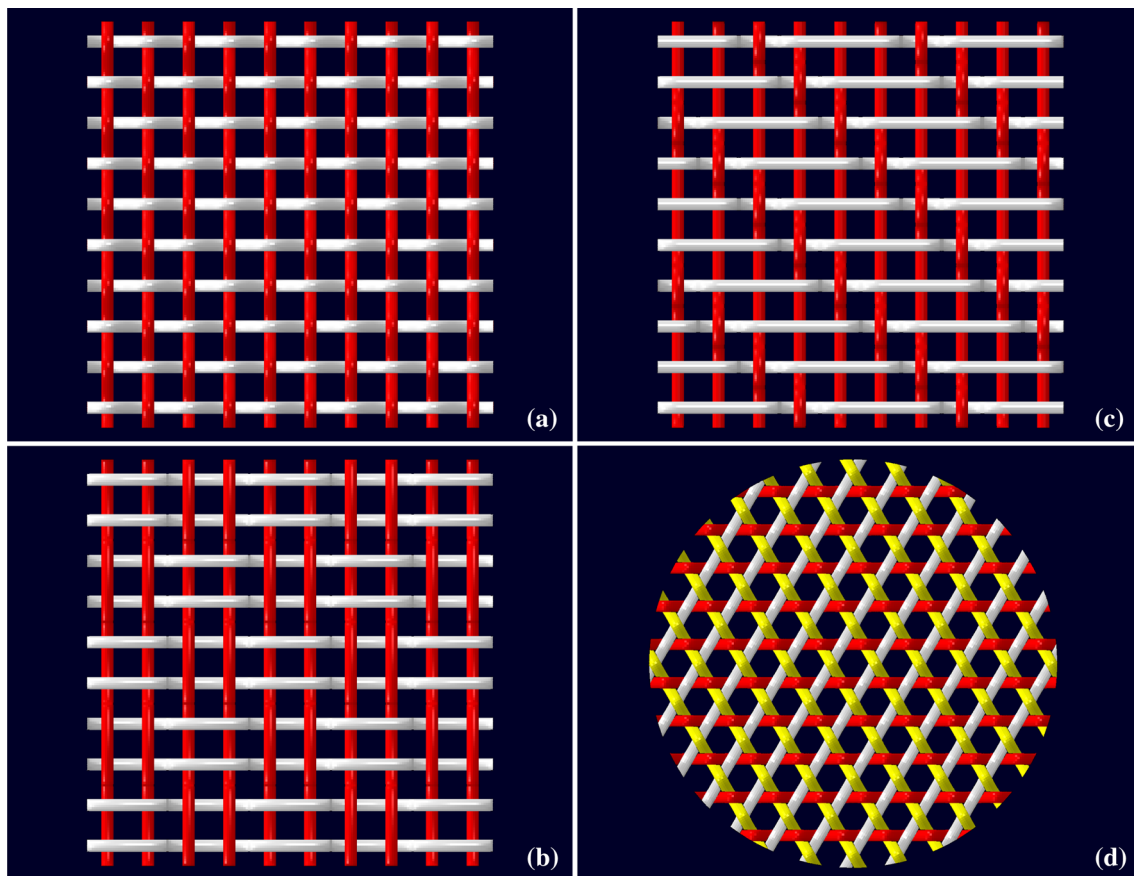


Fig. 1 Most common weaving patterns used in flexible-armor applications: **a** plain; **b** basket; **c** satin; and **d** triaxial

lengthwise direction of the fabric, run from the front to the back of the loom. On the other hand, the weft yarns run orthogonally to the warp yarns, and the two sets of yarns are interlaced.

Typically, the weaving process involves repeated application of the following four basic steps:

- (a) *shedding*—within this step, warp yarns are separated into two groups/sheets, with the pattern of separation depending on the weave architecture, e.g., for a plain-weave, alternating warp yarns are placed into the same sheet. Separation between the two sheets is referred to as shed, and its size has to be sufficiently large to enable the passage of the weft-yarn carrier/shuttle;
- (b) *picking*—within this step, weft/pick yarns are laid between the two warp sheets, i.e., into the shed;
- (c) *beating in*—within this step, a comb-like tool called a reed is used to push weft yarns against the fabric already formed; and
- (d) *taking up and letting off*—within this step, the fabric is being wound onto a cloth-/take-up-roller, while warp yarns are being “let in” from the weaver’s

beam. Strictly speaking, this is not a separate step, but a step that is taking place at a constant rate.

Once one four-step cycle is completed, the action is returned to the shedding step, within which a new shed is formed in accordance with the desired weave architecture. In other words, some or all of the warp yarns previously residing in one sheet are moved to the previous position of the other sheet. In the case of plain-weave, the entire two warp-yarn sheets exchange their places. In this process, the weft-yarn is sandwiched between two sets of crimped/undulated warp yarns, and can experience minor crimping/waviness. This description clearly indicates that warp-yarns experience, in general, more deformation/crimping (and, hence, potentially more damage) during the weaving process, than their weft counterparts. Consequently, when the fabrics are made of ballistic-class yarns, the warp yarns, in the woven fabric, generally possess inferior mechanical properties.

Degradation of weft and warp yarns during weaving

The analysis presented in the previous section clearly revealed that, during the weaving process, yarns (in

particular, the warp yarns) can be subjected to a considerable amount of crimping. Since crimping is a bending process, the largest strains/stresses associated with it reside on the surface of the yarns. When these strains/stresses are sufficiently high, surface damage can be introduced into the yarns, causing degradation in their mechanical properties.

An additional mode of surface damage arises from the fact that during the weaving process, crossing yarns in contact undergo relative sliding. This process can cause surface abrasion in the contacting yarns, another mode of yarn-surface damage. This damage mode can further compromise the structural integrity and mechanical properties of the yarns residing in the woven fabric.

Also, before being used in the weaving process, yarns are often coated for surface protection and, hence, the removal of the coating from the woven fabric requires fabric washing and drying. These processes can also impart some damage (not only of a surface- but also of a bulk-type) within the yarns residing in the woven fabric.

Based on the analysis presented above, the following main observations can be made: (a) yarns residing in the woven fabric possess mechanical properties which are inferior relative to their counterparts in the virgin yarn and (b) the degree of this inferiority is expected to be larger in the warp yarns.

PPTA high-performance fibers/yarns

Since the formulation and construction of the molecular-level PPTA computational models used in the present work entailed detailed knowledge of the basic PPTA chemistry, bonding, crystal, and hierarchical structures and fabrication-induced defects, a brief overview of these material aspects is presented in the remainder of this section.

Class identification

PPTA materials (e.g., Kevlar[®], Twaron[®], Technora[®] etc.) fall into the category of aromatic polyamide or aramid materials.

PPTA molecules/chains

The PPTA repeat units/mers appears in two distinct: (a) *trans* (“on the opposite side”) and (b) *cis* (“on the same side”) molecular-level conformations. These conformations are shown using a ball-and-stick representation in Fig. 2a–b, respectively. To help with interpretation of the molecular structure, the chemical elements are labeled in Fig. 2a. Examination of Fig. 2a–b reveals that the repeat unit consists of two phenylene rings/moieties (C₆H₄RR') connected by an amide linkage (–CO–NH–). Although the PPTA molecule can assume either the *trans* or *cis*

stereo-isomeric conformations, the former conformation is almost exclusively observed. The reason for this predominance is that the *trans* conformation promotes the stretching/extension of PPTA molecules, lowering the system energy. In addition, extended molecules can readily align, forming sheets consisting of nearly parallel, regularly spaced PPTA chains. Formation of these sheets is associated with further reductions in the system energy. Regular stacking of these sheets leads to the formation of low-energy crystalline PPTA fibrils (subfiber units, elongated, and coaxial with the fibers). In sharp contrast, the *cis* conformation hampers the formation of these low-energy structures, which explains its rare occurrence.

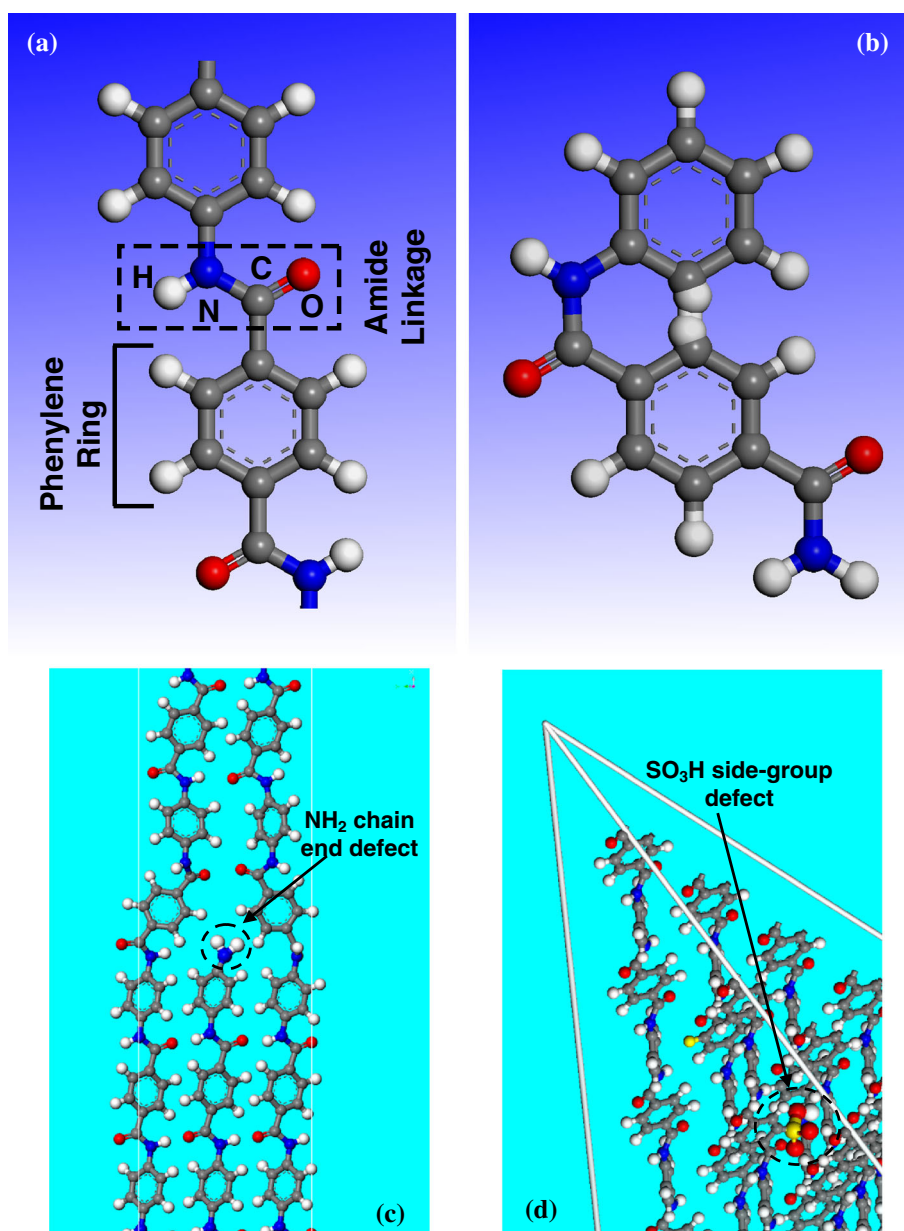
PPTA sheets

Due to a large difference in electronegativity between oxygen and hydrogen, the electron charge density within the PPTA unit cell is increased around the oxygen atoms and lowered around the hydrogen atoms, giving rise to the formation of (relatively strong) dipoles. The presence of dipoles along with (i) the lone electron pairs on the oxygen atoms; (ii) close proximity of the oxygen and hydrogen atoms of neighboring parallel PPTA molecules within the same sheet; and (iii) the operation of London-dispersion forces typically results in the formation of (strong) hydrogen bonds. London-dispersion forces are temporary intermolecular forces which are caused by instantaneous polarization of the interacting molecules due to repulsion of their adjacent electrons [1]. Within the hydrogen bonds, the N–H species acts as a bond donor, while O acts as a bond acceptor. The high strength of hydrogen bonds stems from the covalent-like bonding between the donor and acceptor atoms (accompanying the redistribution of the lone electron-pair charge density), electrostatic attractions between the opposite poles of the neighboring chains, and the development of London-dispersion forces. The formation of the aforementioned sheet-like structures is believed to be the result of strong lateral hydrogen bonding between adjacent parallel PPTA molecules.

PPTA fibrils

As mentioned above, stacking of sheets results in the formation of crystalline fibrils, the axes of which are aligned with the fiber axis. However, orientation of the fibril crystal structure within a plane normal to the fiber axis varies among the fibrils. In other words, PPTA fibrils within a single fiber resemble columnar grains observed in directionally solidified as-cast metallic microstructures. However, in contrast to the columnar metallic grains, the PPTA fibrils are generally found to possess a superstructure consisting of small amplitude (ca. 20 nm), high wavelength

Fig. 2 **a** *Trans*-; and **b** *cis*-molecular conformations in typical PPTA-based polymeric-material molecules/chains; **c** NH_2 -type chain-end; and **d** SO_3H -type side-group defects present in PPTA fibrils/fibers



(ca. 300–500 nm) accordion-style “*pleats*.” The presence of these pleats is often cited as one of the causes for the superior tensile ductility of PPTA fibrils/fibers [e.g., 2]. While intra-sheet bonding is of a strong hydrogen-bonding type, inter-sheet bonding involves weak van der Waals interactions and the formation of π -type molecular orbitals. Thus, PPTA fibrils possess a substantial level of transverse anisotropy.

In addition to the stimulating effect of strong hydrogen bonding, PPTA sheet and fibril formation are also believed to be influenced by the unique molecular (or, more specifically, back bone) structure of PPTA chains, the structure which is associated with a high value of the bending rigidity/stiffness. Specifically, due to limited molecular flexibility and the

absence of molecular folding of PPTA chains, the PPTA fibril/fiber microstructure is not the commonly observed mixture of crystalline and amorphous phases. Rather, the microstructure of PPTA fibrils/fibers is characterized as being either paracrystalline or fully crystalline. While in both structures, molecules are aligned with the fiber axis, the sheets are stacked with a significantly higher degree of regularity in the fully crystalline than in the paracrystalline structure. Another factor often cited as the promoter of the fully crystalline/paracrystalline structure within the PPTA fibrils/fibers is the presence of the planar phenylene and amide groups within the PPTA chains.

As mentioned above, inter-sheet bonding within PPTA fibrils is relatively weak and, consequently, fibrils tend to

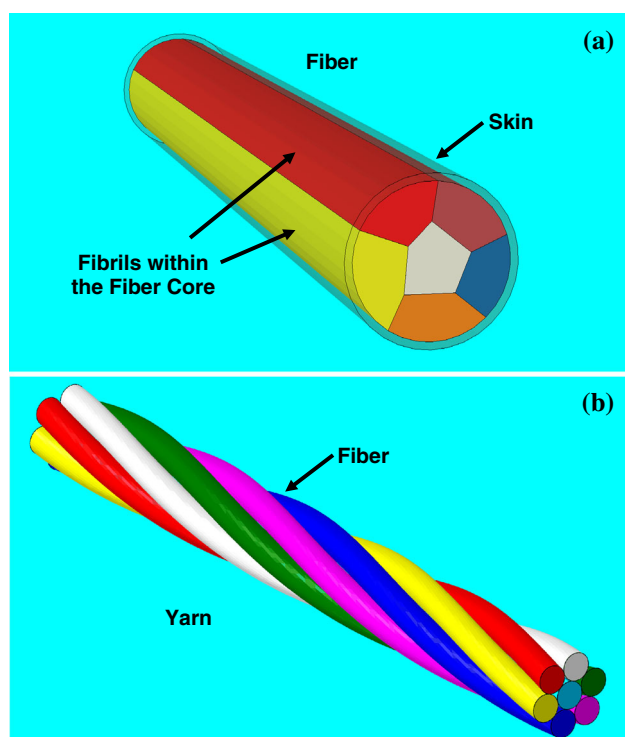


Fig. 3 Topological relationships between: **a** fibrils within a single fiber; and **b** fibers within a lightly twisted yarn

possess various crystallographic and topological inter-sheet defects (e.g., local delaminations [3]). This is the reason that PPTA fibrils tend to buckle during axial and lateral (sheet edge-on) compressive loading, and to possess relatively inferior axial/transverse compressive properties. Weak inter-sheet bonding can also result in increased water absorption, further compromising structural integrity and durability of PPTA fibrils [2].

PPTA fibers

As mentioned above, PPTA fibers are essentially assemblies of parallel fibrils (nearly coaxial with the fiber itself). While it is generally believed that fibril bundles within the fiber are held together by weak van der Waals or Coulomb forces, it is possible that chain cross-linking and the presence of tie-fibrils can play a role in the formation of fibril bundles. While all fibrils contain the same crystalline or nearly crystalline structure, they possess different relative crystallographic orientations. A schematic of the basic architecture of the single PPTA fiber and its relationship to the constituent fibrils is depicted in Fig. 3a. Examination of this figure reveals that the fibril bundles form the fiber core and that the fibers also contain a relatively thin skin region. While this region is comprised of highly oriented PPTA chains, it is usually of a non-crystalline character. It should be noted that, while the schematic displayed in Fig. 3a

shows only six fibrils, actual PPTA fibers typically reveal the presence of hundreds of such fibrils within their core (at a given longitudinal location).

PPTA yarns

PPTA yarns are considered as assemblies of nearly parallel PPTA fibers which are mechanically engaged by either the application of a light twisting to, or by wrapping a fiber around, the fiber assembly. In general, neither of these two ways of yarn fabrication gives rise to a significant damage to the fiber assembly. A schematic of the basic architecture of the single “twisted” PPTA yarn and its relationship to the constituent fibers is depicted in Fig. 3b.

Role of defects/flaws

Since PPTA fibers consist of bundles of nearly parallel and coaxial (fully crystalline or paracrystalline) fibrils, their properties (as is the case for most crystalline materials) are greatly affected by the presence, the type, and the concentration of various crystallographic/topological defects. For example, within the crystalline PPTA fibrils, sheet stacking is typically of an ABABAB type. This stacking is disturbed in the case of paracrystalline fibrils, leading to the formation of higher energy stacking faults. Crystallographic/topological defects do not only affect fiber properties but also the properties and the performance of the coarser-scale structures (e.g., yarns, fabrics, plies, laminae, and laminates). The type, size/potency, and the concentration of these flaws are a sensitive function of the PPTA synthesis and fiber fabrication processes. A summary of the processes of PPTA synthesis and fiber fabrication, as reported in the open literature [4–6], was provided in our recent work [7–12]. The summary clearly established the effect of the synthesis/processing parameters on the type, size, and the concentration of the crystalline and topological defects within the PPTA fibers. In the present work, the effect of two types of PPTA defects, the so-called “chain-end” and the so-called “side-group,” is investigated. Molecular-level structures of two small regions within the PPTA fibril, each containing one of these defects are depicted in Fig. 2c–d. In the case of Fig. 2c, the chain-end is terminated with a NH_2 group, while in the case of Fig. 2d, the inter-sheet side-group consists of a SO_3H molecule.

Prior experimental investigations of weaving-induced yarn damage

Lim et al. [13] investigated the damage induced into the weft and warp PPTA yarns during weaving and the ballistic-penetration resistance of two PPTA yarn-based

fabrics. Their results clearly revealed that (a) the warp yarns extracted from the fabric possess inferior strength properties to their weft counterparts; (b) the extent of warp-yarn strength degradation increases with the linear density of the weft yarns. This observation was linked to the fact that, as the linear density of the weft yarns increases, the extent of warp-yarn crimping/waviness (and, hence, damage) also increases; and (c) the ballistic performance of the fabric initially increases, and peaks then begins to degrade as the weft-yarn linear density increases. These findings have been rationalized by the fact that initially the effect of added weft yarns has a dominant effect, while at higher values of the weft-yarn linear density, the effect of warp-yarn degradation begins to prevail. In other words, there is an optimum value of the weft-yarn linear density associated with the maximum ballistic-penetration resistance of the fabric.

Sanborn et al. [14] compared the mechanical behavior of warp and weft yarns extracted from plain-woven Kevlar KM2 (a commercial grade of PPTA) fabric with the corresponding reference/non-woven yarns. Quasi-static and intermediate rate experiments were conducted using a Bose ElectroForce Test System, while high-rate performance was measured using a miniature tension Kolsky bar. The results obtained revealed that (a) warp yarns possess inferior strength properties with respect to the reference yarns and (b) the weft yarns, in a statistical sense, possess the same strength properties as the reference yarns.

Rocher et al. [15] investigated the extent of weaving-induced strength degradation in fabrics made of hybrid polypropylene/glass yarns, at different testing strain rates. The results obtained relatively little damage (and, hence, strength degradation) in weft yarns. On the other hand, the fracture strength and Young's modulus of the warp yarns were reduced, on average, by 28 and 17 %, respectively, relative to their reference/non-woven counterparts. The work also showed that as the linear density of the weft yarns increases and, hence, the extent of warp-yarn crimping increases, the strength and stiffness degradations in the warp yarn also increase.

Hunt et al. [16, 17] carried out an extensive investigation of the degradation of warp and weft yarns during the fabric-weaving process, as well as the degradation of through-the-thickness yarns used for stitching multi-ply fabric structures. A variety of yarns were examined, including Dyneema [highly oriented ultra-high molecular weight polyethylene (UHMWPE) filaments], Vectran (polyester), S-2 glass, Kevlar KM2, etc. The results obtained clearly established that (a) the dominant strength-degrading mechanism may differ from one yarn type to the other. For example, in Kevlar KM2 and Vectran, the crimping-induced damage, in the form of kink bands (primarily in the warp yarns), has the prevailing effect.

On the other hand, in Dyneema, surface abrasion appears to be the dominant fabric-fabrication process-induced yarn strength-degradation mechanism; (b) in multi-ply fabric structures, through-the-thickness stitching yarns may experience even larger strength degradation than warp yarns during fabric-weaving; and (c) among the yarns investigated, Dyneema appears to have the highest strength retention when used as cross-stitching yarn.

Main objective

The two main objectives of the present work are (a) to quantify computationally the effect of prior compressive and tensile (bending) stresses on the longitudinal-tensile strength of PPTA fibers using coarse-grained molecular methods and tools and (b) to assess the extent of strength degradation experienced by the warp and weft yarns during the plain-weaving process, by carrying out a simplified finite-element analysis of this process.

Paper organization

Details regarding the coarse-grained techniques used including the construction of the computational model, formulation and parameterization of the force-fields, computational algorithms, problem formulation, post-processing data-reduction analyses, and the key results obtained are all presented in “[Coarse-grained fiber-scale computational analysis](#)” section. The finite-element analysis (including the results) of the plain-weaving process and the accompanying degradation in the warp-/weft-yarn strengths is described in “[Finite-element analysis \(FEA\) of plain-weaving process](#)” section. The key findings resulting from the present work are summarized in “[Conclusions](#)” section.

Coarse-grained fiber-scale computational analysis

As mentioned earlier, coarse-grained fiber-scale computational methods have been employed in the present work in order to investigate degradation in the PPTA fiber/yarn tensile strength, as a result of the prior compressive or tensile loading. PPTA fibers/yarns experience this type of loading in the course of the plain-weaving fabric-manufacturing process.

Within the coarse-grained computational framework, atoms, ions, and inter-atomic bonds are not modeled explicitly but rather, individual atoms/ions are combined into larger single particles, referred to as “*beads*,” where each bead represents the collective degrees of freedom of the constituent atoms/ions. Neighboring beads residing within the same chain are then connected using bead/bead

bonds (also referred to as connectors), while non-bonded beads are allowed to interact via van der Waals-like and Coulomb-like force-fields (the term “*force-field*” will be defined later). Since the coarse-grained computational framework employs larger particles (relative to the particle sizes encountered in the so-called all-atom computational analyses), larger computational domains can be analyzed (simulating the maximum number of particles permitted by the available computational and storage resources). In addition, by integrating out the high-frequency vibrations of the constituent atoms/ions and allowing the system dynamics to be controlled by the compliant/soft, bead/bead interactions (rather than by stiff/hard, atom/atom interactions), a significantly longer time scale is attained (relative to that which could be afforded by the all-atom computational method).

It should be noted that, while only coarse-grained molecular methods and tools are used in the present work, the results of the all-atom molecular-dynamics simulations carried out in our recent work [7–11] were utilized. Specifically, all-atom molecular-dynamics calculations described in Refs. [7–11] were used (a) to identify the nature and the number of types of coarse-grained beads; (b) for each bead type, to quantify the bead mass and bead size; and (c) to help parameterize intra- and inter-chain coarse-grained force-fields (a set of mathematical expressions describing various contributions to the potential energy function for the system of interacting particles, i.e., beads, in the present case). A brief description of the all-atom computational procedures employed in our recent work [7–11], and of the associated results used in the present work, is provided below.

PPTA coarse-graining and force-field parameterization

Within the all-atom computational methods, molecular-level models of individual PPTA chains based on the *trans* molecular conformation of the repeat unit, Fig. 2a are constructed using the Visualizer [18] program from Accelrys. Typically, PPTA chains consisting of 20 repeat units and having the molecular weight of ca. 4760 Da are used. Atom/atom bonding and non-bonding interactions are quantified using the so-called “COMPASS” (Condensed-phase Optimized Molecular Potentials for Atomistic Simulation Studies) force-field [19, 20]. This highly accurate force-field is of an *ab initio* type since most of its parameters were determined by matching the predictions made by the *ab initio* quantum mechanics calculations to the condensed-matter experimental data. The force-field defines mathematical expressions for the energy contribution of, and the force acting upon, a bead as a function of its local environment (i.e., the nature, the position, and the bond status of the neighboring beads).

PPTA coarse-graining

Since PPTA can be considered as a homopolymeric material, and in order to be able to handle computational domains of a larger size, only one type of bead is introduced during the coarse-graining procedure of the PPTA chains. Consequently, the bead mass was set equal to that of the PPTA repeat unit while the volume allotted to each bead was readily derived from the PPTA-fiber mass density.

Coarse-grained force-field functions

The coarse-grained force-field used in the present work includes four (functionally distinct) contributions to the system potential energy: (a) intra-chain bond-stretch term; (b) inter-chain two-bond-angle term; (c) intra-sheet hydrogen-bond term; and (d) inter-sheet van der Waals non-bond interaction term. The functional forms for the four potential-energy terms are given below:

Intra-chain bond-stretch term Covalent bonding within the bead type PPTA chains is represented using the following form of a harmonic-type energy function:

$$E^{\text{stretch}} = \frac{1}{2} K^{\text{stretch}} (r - r_o^{\text{stretch}})^2, \quad (1)$$

where K^{stretch} denotes the bond-stiffness parameter, r the connector (i.e., bead bond) length, and the subscript o is used to denote the equilibrium value of the associated quantity. Due to the high stretching stiffness of the PPTA molecules, K^{stretch} is assigned a relatively large value, as will be shown later. It should be noted that the bond-stretch term describes interactions between two covalently bonded beads using a linear axial spring model.

Intra-chain two-bond-angle term An analogous harmonic function is used to represent the potential energy contribution associated with the intra-chain two-bond-angle term as follows:

$$E^{\text{angle}} = \frac{1}{2} K^{\text{angle}} (\theta - \theta_o^{\text{angle}})^2, \quad (2)$$

where K^{angle} denotes the bond-stiffness parameter and θ the intra-chain inter-bond angle. Due to the high bending rigidity of the PPTA molecules, θ_o^{angle} is set to a value of π , while as will be shown later, K^{angle} is assigned a relatively large value. It should be noted that the two-bond-angle term describes interactions between two pairs of covalently bonded beads sharing a bead using a linear torsional spring model.

Intra-sheet hydrogen-bond term: Following our prior work on polyurea [21–23], the potential energy associated with intra-sheet inter-chain hydrogen bonding is expressed using the 18-9 Lennard-Jones type of function as

$$E^{\text{hydrogen}} = \varepsilon^{\text{hydrogen}} \left[\left(\frac{r_0^{\text{hydrogen}}}{r} \right)^{18} - 2 \left(\frac{r_0^{\text{hydrogen}}}{r} \right)^9 \right], \quad (3)$$

where $\varepsilon^{\text{hydrogen}}$ is the interaction energy minimum and represents the strength of hydrogen-bond interaction between two beads, while r_0^{hydrogen} is the associated hydrogen-bonded inter-bead equilibrium distance.

Inter-sheet van der Waals non-bond interaction term As far as the non-bond van der Waals interaction energy involving beads residing on different PPTA sheets is concerned, it is represented using the 12-6 Lennard-Jones type of function as

$$E^{\text{non-bond}} = \varepsilon^{\text{non-bond}} \left[\left(\frac{r_0^{\text{non-bond}}}{r} \right)^{12} - 2 \left(\frac{r_0^{\text{non-bond}}}{r} \right)^6 \right], \quad (4)$$

where $\varepsilon^{\text{non-bond}}$ is the interaction energy minimum and represents the strength of non-bond interaction between two beads, while $r_0^{\text{non-bond}}$ is the associated non-bonded inter-bead equilibrium distance.

Coarse-grained force-field parameterization

Procedures used for parameterization of each of the four parts of the coarse-grained force-field are presented in this section.

Intra-chain bond-stretch term: Since the coarse-grained formulation used in the present work defines only one type of bead, the bond-stretch force-field term contains only two parameters: K^{stretch} and r_0^{stretch} . r_0^{stretch} was determined by setting it equal to the equilibrium bead/bead separation, as computed using all-atom molecular statics calculations of the minimum potential-energy configuration of a single infinitely long, perfectly straight PPTA chain.

To determine K^{stretch} , an equilibrium molecular-dynamics-based free-energy calculation procedure is combined with the so-called “Adaptive Biasing Force” (ABF) method [22]. During the application of the ABF method, the distance between the centers of mass of the (all-atom represented) beads is varied in small increments from its initial (minimum energy) value by appropriately changing the relative position of all constituent atoms. This was followed by prolonged (40-ns simulation time, at a temperature of 300 K) all-atom equilibrium molecular-dynamics simulations. The trajectory results obtained, averaged over the simulation time, are used to compute the mean force acting on the beads, quantifying the tendency of the beads’ connector to recover its equilibrium length. To cancel this force, a biasing force of equal magnitude and opposite sign is equally partitioned and applied to all the constituent atoms in the two beads. This leaves the system under zero mean force and only the fluctuating part of the force remains, enabling the computation of

the “equilibrium” thermodynamic properties of the system, e.g., mean potential energy at a given value of the bead connector length. When the resulting potential energy versus connector length results are fitted using linear regression analysis in conjunction with Eq (1), the sought-after stretching stiffness parameter is obtained. The resulting functional relationship for bond-stretch energy versus bonded-bead separation is depicted in Fig. 4a.

Intra-Chain Two-Bond-Angle Term The two-bond-angle force-field term also contains only two parameters: K^{angle} and θ_0^{angle} . As mentioned earlier, θ_0^{angle} is set to a value of π . As far as the bending stiffness parameter K^{angle} is concerned, it is determined using an ABF-based-procedure analogous to that described for the case of K^{stretch} . The main difference is that instead of a perfectly straight PPTA molecule, a molecule consisting of two perfectly straight halves with an included angle θ (of varying magnitude) is utilized. The resulting functional relationship for bond-angle energy versus two-bond-angle is depicted in Fig. 4b.

Intra-sheet hydrogen-bond term Due to the presence of a single bead type, the hydrogen-bond part of the coarse-grained force-field is also characterized by two parameters: $\varepsilon^{\text{hydrogen}}$ and r_0^{hydrogen} . These two parameters were determined using the same procedure as the ones described above, except that instead of a single infinitely long, perfectly straight chain, a wall of parallel, equally spaced, infinitely long, perfectly straight chains is used, and the inter-chain spacing is varied. The resulting functional relationship for hydrogen-bond energy versus intra-sheet inter-chain separation distance is depicted in Fig. 4c.

Inter-sheet van der Waals non-bond interaction term The two non-bond interaction parameters $\varepsilon^{\text{non-bond}}$ and $r_0^{\text{non-bond}}$ are determined using the same procedure, except that an infinitely wide/deep/tall stack of PPTA sheets (with the ABABAB... stacking), each consisting of an array of parallel, equally spaced, infinitely long, perfectly straight chains, is used. The resulting functional relationship for non-bond energy versus inter-sheet separation distance is depicted in Fig. 4d.

Parameterization Summary A summary of the eight coarse-grained PPTA force-field parameters is provided in Table 1.

Coarse-grained molecular method

All-atom and coarse-grained molecular methods and tools are fundamentally identical, since both treat materials as assemblies of interacting particles and use force-fields to quantify various bonding and non-bonding interactions. The two main differences between the two methods are (a) the nature, and size/mass, of the constituent interacting (atoms vs. beads) particles and (b) bead/bead interactions are generally quite more compliant (softer) than their atom/atom counterparts.

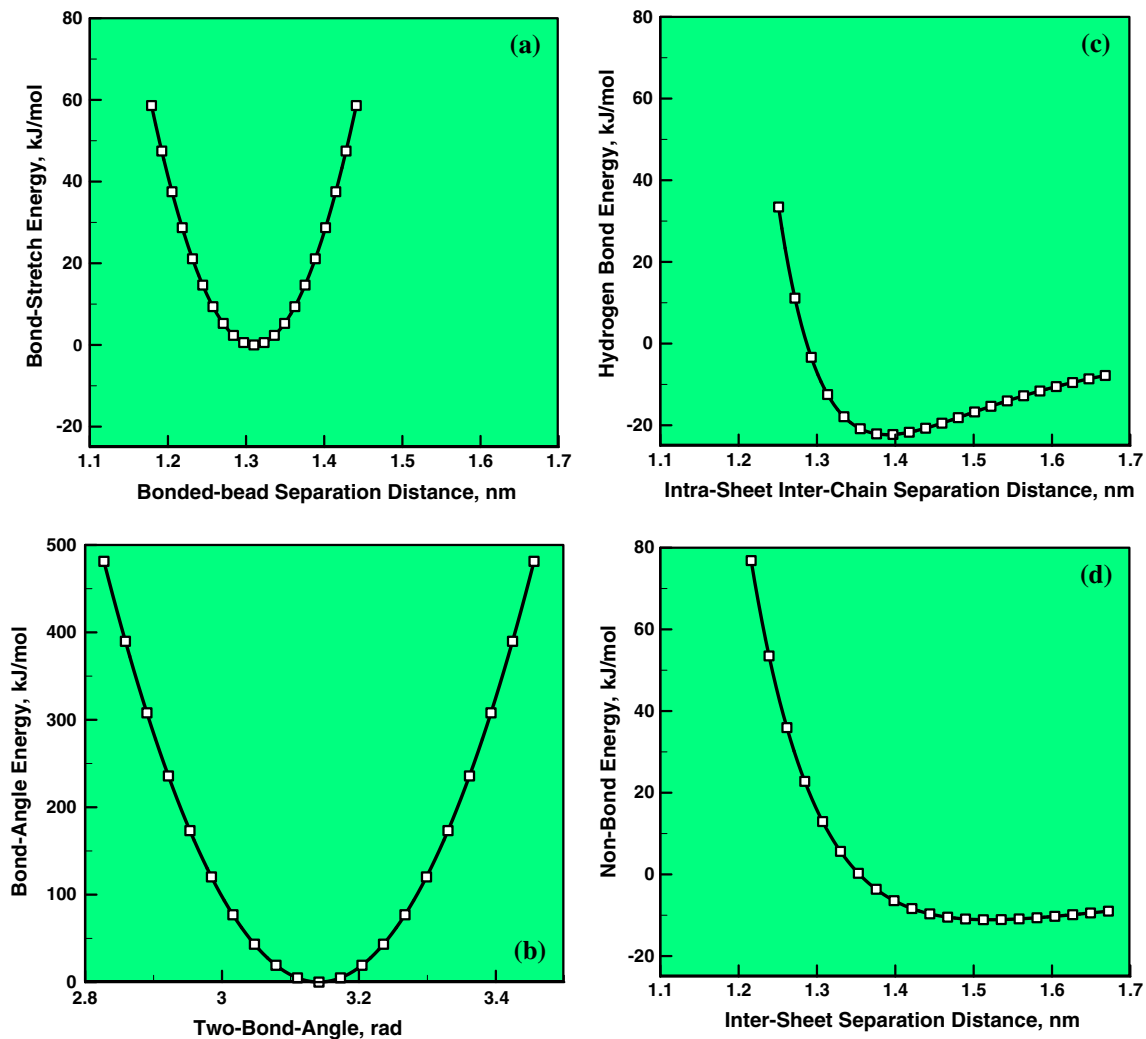


Fig. 4 Coarse-grained PPTA force-field functions used in the present work: **a** bond-stretch term; **b** two-bond-angle term; **c** hydrogen-bond term; and **d** non-bond term

Table 1 Coarse-grained PPTA force-field parameterization used in the present work

Parameter	Unit	Value
K^{stretch}	kJ/mol nm ²	6831.1
r_o^{stretch}	nm	1.31
K^{angle}	kJ/mol rad ²	9752
θ_o^{angle}	rad	π
$\epsilon^{\text{hydrogen}}$	kJ/mol	22.3
r_o^{hydrogen}	nm	1.39
$\epsilon^{\text{non-bond}}$	kJ/mol	11.1
$r_o^{\text{non-bond}}$	nm	1.52

Please see Eqs. (1)–(4) for explanation of the symbols

In general, a complete formulation of a coarse-grained molecular simulation problem includes, at a minimum, the following four items: (a) a computational model consisting

of bead-type chains and larger structures (e.g., sheets, fibrils, fibers, etc.); (b) a set of inter-bead force-field potentials which describe accurately various bonding and non-bonding bead/bead interactions; (c) a computational method(s) to be used in the simulations; and (d) formulation of the problem to be analyzed. These four items are discussed in greater detail in the remainder of this section.

Computational model(s)

While the coarse-grained computational approach allows a substantial increase in the dimensions of the computational cell analyzed, a coarse-grained analysis of a segment of the PPTA fiber (typical diameter on the order of 10 μm) would still require the use of a prohibitively large number of beads. Considering the fact that a majority of the crystalline/topological defects are located in the core of the PPTA

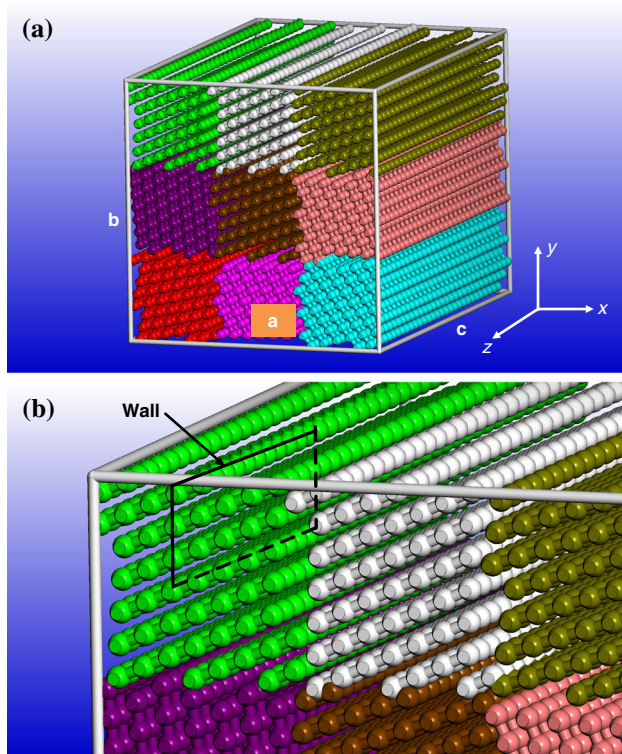


Fig. 5 Coarse-grained PPTA fiber computational cell consisting of nine coaxial fibrils (indicated using different colors): **a** zoomed-out view; and **b** a close-up view

fibers, and that these defects play an important role in the kink-band nucleation process (discussed later), the computational domain used focuses on the core-section of the PPTA fibers. Furthermore, since the transverse cross-section of the computational domain is still small in comparison to that of the PPTA-fiber core, the computational domain is assumed to extend indefinitely in the lateral directions (as well as in the axial direction). The rectangular-parallelepiped-shaped computational cell used in the present work is shown in Fig. 5a. The long edge, c , of the computational cell is aligned with the fiber axis (which is, in turn, aligned with the z -coordinate axis). The remaining two transverse edges (a and b) of the cell are aligned, respectively, with the coordinate axes x and y . Typically, computational cells of the size $a = 24.3$ nm, $b = 24.3$ nm, and $c = 28.6$ nm are used. The infinite extension of the computational domain in the three orthogonal directions is achieved by applying the periodic boundary conditions across the computational cell faces. It should be noted that the dimensions of the computational cell used are a compromise between a lower computational cost (which favors a smaller computational cell) and the magnitude of the effect of the computational cell size on the material strength (which favors a larger computational cell). In other words, the present computational cell sizes enabled

analysis of the material strength/stiffness behavior at a relatively low computational cost, while ensuring that further increases in the computational cell size would not yield significantly different quantitative results.

Examination of the transverse cross-section of the computational cell shows that the cell consists of nine coaxial fibrils (identified by different colors). While each fibril contains the same PPTA crystal structure, the transverse orientation of this structure differs among the fibrils. However, in all fibrils, the orientation of the crystal lattice is such that the sheet normal is orthogonal to the fiber axis. The initial atomic (or, more precisely, the bead) configuration was constructed while obeying the basic crystallographic relationships within the PPTA phase. Toward that end, the mean mass density within each fibril is initially set to be the same (by properly adjusting inter-chain distances within the sheets and inter-sheet distances) for each fibril. To equilibrate the initial configuration, before conducting any analysis/testing of the computational cell, the potential energy of the computational cell is minimized with respect to the spatial coordinates of the constituent beads. It should be noted that the atomic configuration displayed in Fig. 5a is the initial (before energy minimization) configuration. A close-up of this configuration is displayed in Fig. 5b. This figure clearly shows the formation of PPTA sheets which contain covalent intra-chain bonds and inter-chain, intra-sheet hydrogen bonds (both depicted using the ball-and-stick representation).

Force-fields

The force-field functions used, the procedure employed for their parameterization and the resulting parameters' identification were all covered in “PPTA coarse-graining and force-field parameterization” section and, hence, will not be repeated here.

Computational method(s)

Within the coarse-grained fiber-scale computational investigation carried out in the present work, two types of computational methods, molecular statics (i.e., potential-energy minimization) and (equilibrium) molecular dynamics (i.e., particle-trajectory analysis), are used. These methods are implemented in Discover (a general-purpose atomistic simulation program) from Accelrys [24], the computational tool which was employed in the present work. Within the molecular statics approach, the potential energy of the subject discrete-particle material system is minimized with respect to the position of the particles/beads. On the other hand, within the molecular-dynamics approach, gradient of the potential energy (as defined by the force-field functions) with respect to the particle

positions is first used to generate forces acting on the particles and, then, the associated Newton's equations of motion (for all particles) are integrated numerically in order to determine the temporal evolution of the particle positions (i.e., particle trajectories). In addition, within the equilibrium molecular-dynamics methods, the system under consideration is coupled to an (external) environment (a constant temperature reservoir, in the present case) which ensures that the system remains in thermodynamic equilibrium (i.e., the system does not experience fluxes of thermodynamic quantities). In the present work, an NVT (where N is the (fixed) number of atoms, V is the computational cell volume (also fixed), and T (≈ 300 K) is the temperature) rendition of the molecular-dynamics method is employed.

As will be shown in the following, combined application of the molecular statics and equilibrium molecular-dynamics methods enables the investigation of (a) behavior of the PPTA fiber core under axial-compressive/tensile loading; (b) formation of loading-induced defects such as kink bands; and (c) elucidation of the interplay between various fiber-processing-induced crystallographic/topological defects and the propensity of the material to generate additional defects (e.g., kink bands during loading). All the calculations in the present work were carried out by coupling a user-defined coarse-grained force-field database with the Discover solver [24]. The procedure employed to simulate PPTA-fiber axial compression or extension is implemented and linked with Discover through the use of an input file written in the BTCL script. This enabled precise control of all simulation tasks such as sequential contraction or expansion of the computational cell in the longitudinal direction (during the simulation of the axial-compression/-tension test).

Problem formulation

As mentioned earlier, the problem analyzed in the present work involves determination of the functional relationship between the extent of material degradation and longitudinal-tensile-strength loss in PPTA fibers, as a result of the prior compressive or tensile axial loading. In a typical coarse-grained axial loading analysis of the PPTA fibers, both the preludial compression/tension and the subsequent longitudinal tension are applied in small increments and each incremental deformation is followed by the computational cell energy minimization and extended (ca. 40 ns) molecular-dynamics simulation runs.

Post-processing data-reduction analysis

The coarse-grained fiber-level particle-trajectory computational results obtained are mainly used to reveal the

response of single PPTA fibers to uniaxial compression/tension (including the microstructural/topological evolution processes such as kink-band formation and fibrillation). Fiber axial compression/tension is simulated by subjecting the unit cell to longitudinal compressive/tensile deformation in the z -direction, while allowing for the operation of the Poisson's effects in the x - and y -directions. In other words, at each incremental uniaxial compression/tension strain, the lateral dimensions of the cell are adjusted, while preserving the periodic boundary conditions, until the normal stresses in the lateral directions became effectively zero. In the case of preludial axial compression/tension, except for using the trajectory data for graphical display, no data post-processing procedure had to be employed. However, the pre-loaded/unloaded computational cells were subsequently subjected to tensile reloading in order to assess the extent of longitudinal-tensile strength (and Young's modulus) loss during preludial loading. In these cases (a) following uniaxial compression/tension and the formation of deformation-induced defects such as kink bands or fibrillation, the unit cell is subjected to longitudinal-tensile deformation while allowing for the operation of the Poisson's effects in the transverse directions; and (b) the trajectory data had to be post-processed to extract and quantify the effect of preludial loading. During tensile reloading, the procedure described in our recent work [21] was utilized to compute the normal axial stress and its rate of change with an increase in the axial tensile strain. The longitudinal-tensile strength of the single PPTA fibril is then set equal to the value of the corresponding normal stress at which the rate of stress increases with increase in strain begins to decline "*appreciably*" (denoting the onset of inelastic-deformation and/or damage-initiation processes).

Results of the coarse-grained analysis

As established in the Introduction section, PPTA fibrils/fibers contain a variety of synthesis/processing-induced crystallographic/morphological defects which control their mechanical properties. Consequently, the hypothetical case of crystallographically perfect PPTA fibrils/fibers has not been investigated in the present work. In our recent work [7–11], a detailed overview was provided with respect to the character of the main microstructural/topological defects found in PPTA fibers, their classification, their origin in relation to the PPTA synthesis/processing conditions, and their (estimated) typical concentrations. Therefore, a similar detailed overview will not be provided here. Nevertheless, it should be noted that the prior work [7–11] clearly established that among the isolated and clustered point-type defects, the following has the largest effect on the PPTA fibril/fiber properties (in particular, on the

longitudinal-tensile strength): (a) chain-ends; (b) side-groups; and (c) voids and interstitials. In addition, planar-type defects, commonly referred to as defect bands, were also found to have a major effect on the fibril/fiber strength. In the present work, only the effect of (isolated or clustered) chain ends or side-groups was investigated. Chain ends are the defects which stem from the fact that some of the fibril chains do not run continuously along the fiber length but rather terminate (at one or both ends) within the fiber. As far as the side-group defects are concerned, they are associated with the presence of radicals, e.g., $-\text{SO}_3\text{H}$, $-\text{SO}_3^-\text{Na}^+$, between the PPTA sheets. As shown in our previous work [7–11], the presence of these two types of defects and their clusters within the (otherwise) perfect PPTA fibers causes local changes in the material microstructure. These microstructural changes, as will be shown below, are the root cause of the reduced longitudinal-tensile strength in the as-synthesized PPTA fibers.

Microstructure evolution during axial compression of defective PPTA fibers

Evolution of the coarse-grained microstructure, during axial compression, within the computational cell containing (initially) as-synthesized PPTA fibers having chain-end defects, is depicted in Fig. 6a–d. The longitudinal stretch values associated with Fig. 6a–d are (a) 0.975; (b) 0.950; (c) 0.925; and (d) 0.900. The lateral stretches, in each case, take on the values required by the zero-lateral-stress condition. Examination of the results displayed in Fig. 6a–d clearly reveals formation and subsequent growth/thickening of two counterbalancing non-parallel shear bands. In most cases, removal of the axial-compressive loading did not result in complete disappearance of the kink bands, indicating permanent damage induced into the PPTA fibers by the preludial longitudinal compression. It should be noted that while the results displayed in Fig. 6a–d appear to violate the periodic boundary condition imposed in the lateral directions, they are fully consistent with this type of boundary condition. In other words, the material protruding through the right face of the computational cell displayed in these figures is missing at the corresponding left section of the computational cell. Due to the chosen orientation of the unit cell, selected in such a way as to emphasize the formation of the counterbalancing shear bands protruding outside the right face of the computational cell, the corresponding “void” portion of the unit cell at its left side is not seen.

When isolated or clustered side-group defects are introduced into the PPTA fiber, axial compression is not accompanied by the formation of well-defined kink bands. Rather, microstructural changes resembling fibrillations (flow-induced chain/fibril buckling/localized bending) were observed. An example of the microstructural

evolution during axial compression of PPTA fibers containing side-group defects is depicted in Fig. 7a–d. The longitudinal stretch values associated with Fig. 7a–d are (a) 0.975; (b) 0.950; (c) 0.925; and (d) 0.900. The lateral stretches again, in each case, take on the values required by the zero-lateral-stress condition. Examination of the results displayed in these figures reveals the formation of bulges (an indication of the operation of fibrillation processes) at the computational-cell lateral faces. The height and the breadth of these bulges increase in the course of axial compression. In most cases analyzed, microstructural changes experienced, during preludial compression, by the PPTA fiber containing side-group defects were permanent. That is, with the exception of minor elastic-relaxation processes, removal of the compressive loading did not restore the original/uncompressed microstructure.

Microstructure evolution during axial tension of defective PPTA fibers

Evolution of the coarse-grained microstructure, during axial tension, within the computational cell containing (initially) as-synthesized PPTA fibers having chain-end defects, is depicted in Fig. 8a–d. The longitudinal stretch values associated with Fig. 8a–d are (a) 1.025; (b) 1.050; (c) 1.075; and (d) 1.100, while the corresponding lateral stretches take on the values required by the zero-lateral-stress condition. Examination of the results displayed in Fig. 8a–d clearly reveals that the distributions of the lateral strains within one of the fibrils are not uniform. Rather, there is a localization of the lateral strains in a region adjacent to the pre-existing chain-end defect. In most cases, removal of the axial-tensile loading did not result in complete disappearance of the localized-deformation region, indicating permanent damage induced in the PPTA fibers by the preludial longitudinal tension.

When isolated or clustered side-group defects are present in the PPTA fiber, axial tension does not introduce observable non-uniformities or defects. Consequently, no results pertaining to the microstructural evolution during axial tension of PPTA fibers containing side-group defects are shown.

Longitudinal-tensile strength of the defective as-synthesized PPTA fibers

In our prior work [7–11], it was clearly demonstrated that the longitudinal-tensile strength of the as-synthesized PPTA fibers is highly sensitive to the presence, type, and cluster size of the microstructural/topological defects. Due to the stochastic nature of the spatial distribution of the defect concentration within the fiber, the longitudinal-tensile strength of the fibers has also been found to be a

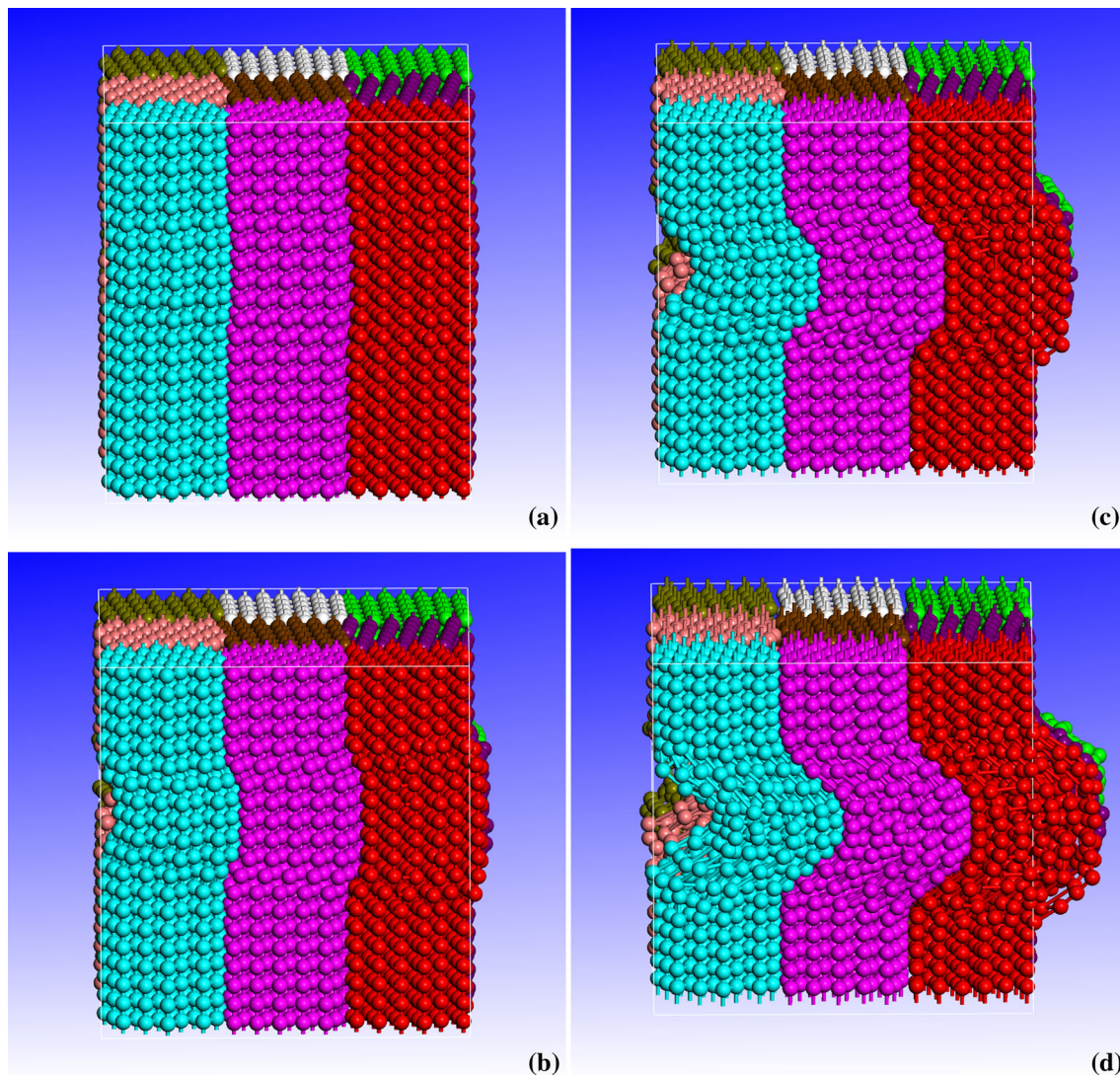


Fig. 6 Evolution of the coarse-grained microstructure, during axial compression, within the computational cell containing (initially) as-synthesized PPTA fibers having chain-end defects. Longitudinal stretch values: **a** 0.975; **b** 0.950; **c** 0.925; and **d** 0.900

stochastic quantity. This finding is in full agreement with several experimental reports (e.g., [25–27]). In our recent work [8], a procedure was introduced for the derivation and parameterization of a probability density function for the longitudinal-tensile strength of the as-synthesized PPTA fibers. Application of this procedure yielded the defective as-synthesized PPTA-fiber longitudinal-tensile-strength probability density function, depicted in Fig. 9. The mean value of the defective as-synthesized PPTA longitudinal-tensile strength, computed as the first moment of the probability density function displayed in Fig. 9, is found to be ~ 5.0 GPa. This value is in reasonably good agreement with the measured PPTA-fiber longitudinal-tensile strength (typically found to be in a 3–5 GPa range [e.g., 23, 26]). This finding suggests that the procedure introduced in Refs. [7–11] can reasonably well account for the experimental

observations regarding the PPTA-fiber longitudinal-tensile strength. Similar conclusions can be drawn in regards to the elastic stiffness moduli of the PPTA fibers since the predicted mean values of the longitudinal (345 GPa) and (isotropic) transverse (46 GPa) Young's moduli are in good agreement with their respective experimental counterparts (350 and 50 GPa) [8].

Residual longitudinal-tensile strength of defective pre-loaded PPTA fibers

The results obtained in the present work pertaining to the residual longitudinal-tensile strength of the pre-compressed or pre-tensioned PPTA fibers containing the two types of synthesis-induced microstructural/morphological defects (i.e., chain-end and side-group) established that (a) the

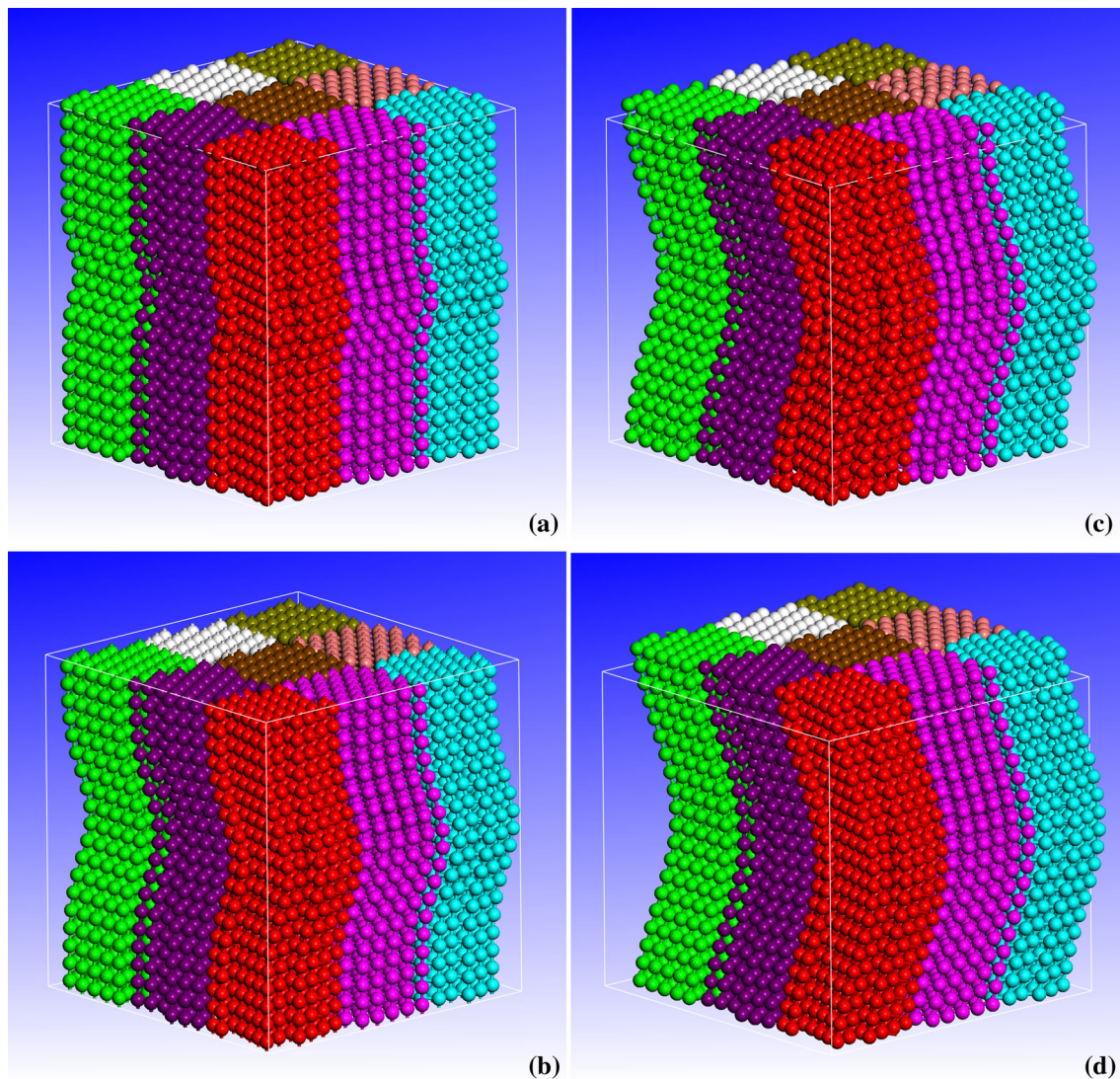


Fig. 7 Evolution of the coarse-grained microstructure, during axial compression, within the computational cell containing (initially) as-synthesized PPTA fibers having side-group defects. Longitudinal stretch values: **a** 0.975; **b** 0.950; **c** 0.925; and **d** 0.900

associated longitudinal-tensile strength probability density function does not undergo a substantial change in its shape relative to its as-synthesized counterpart depicted in Fig. 9; (b) the mean value of the pre-loaded longitudinal-tensile strength probability density function is reduced relative to its as-synthesized counterpart; and (c) the extent of the mean longitudinal-tensile strength reduction is a function of both the nature of the pre-existing microstructural/morphological defects (chain-ends vs. side-groups) and the character of pre-loading (compression vs. tension).

Examples of the results obtained in this portion of the work are shown in Fig. 10a–b. These figures show the percent loss of the (initial) mean fiber longitudinal-tensile strength, as a function of the magnitude of the preludial longitudinal strain. Figure 10a pertains to the case of preludial compression, while Fig. 10b pertains to the case

of preludial tension. In both figures, two curves are shown: one corresponding to the case of defective fibers containing chain-ends, while the other corresponds to the case of defective fibers containing side-groups. It should be noted that non-zero values of the percent loss in the fiber tensile strength are seen at zero values of the preludial compressive/tensile strain. The reason for this is that the fabrication-induced defects (i.e., chain-ends and side-groups) present in the PPTA fiber give rise, themselves, to a reduction in the material strength relative to that found in the defect-free material. In other words, the values of the percent loss in the longitudinal-tensile strength are defined with respect to the longitudinal-tensile strength of defect-free PPTA fibers. Examination and comparison of the results displayed in Fig. 10a–b reveal that (a) preludial longitudinal compression gives rise to a greater loss in the

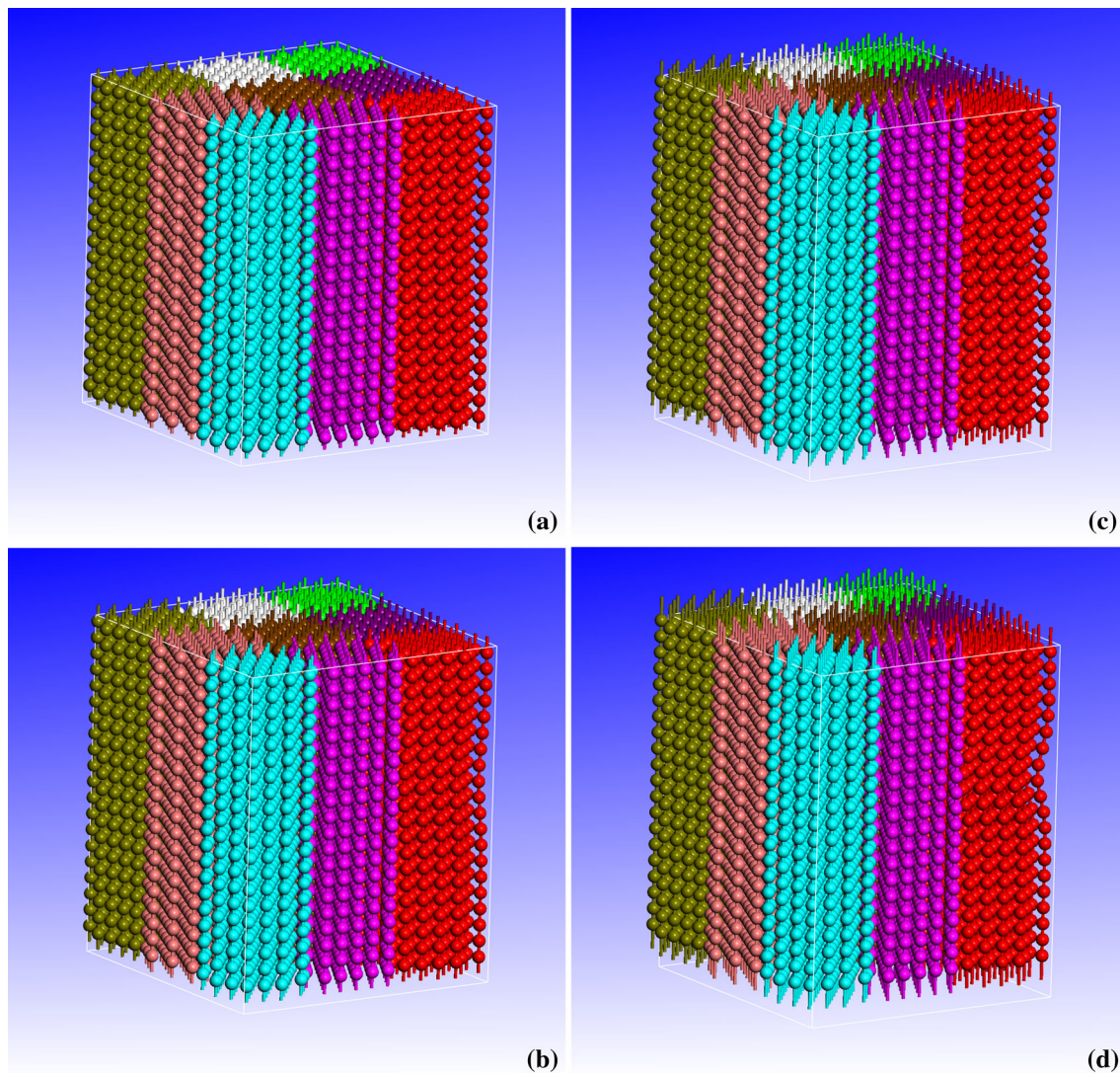


Fig. 8 Evolution of the coarse-grained microstructure, during axial tension, within the computational cell containing (initially) as-synthesized PPTA fibers having chain-end defects. Longitudinal stretch values: **a** 1.025; **b** 1.050; **c** 1.075; and **d** 1.100

fiber longitudinal-tensile strength than preludial longitudinal tension; (b) in the case of preludial compression, side-groups appear to cause a greater degradation in the fiber longitudinal-tensile strength than the chain-ends; (c) contrarily, in the case of preludial tension, chain-ends appear to cause a greater degradation in the fiber longitudinal-tensile strength than the side-groups; and (d) overall, the largest loss in the fiber longitudinal-tensile strength is encountered in the case of preludial longitudinal compression and the pre-existing side-group defects.

Finite-element analysis (FEA) of plain-weaving process

The results obtained in the previous section are used to enrich the PPTA-fiber/-yarn material model developed in our prior work [28–30]. Specifically, the results obtained

are used to parameterize the progressive damage model developed in Ref. [28–30]. Toward that end, the results presented in Fig. 10a–b are weighted by the concentrations of the two microstructural/topological defects, in order to arrive at the overall percent loss of longitudinal-tensile strength versus preludial (compressive or tensile) strain curves, Fig. 10c. Following the procedure outlined in Refs. [28–30], the concomitant loss in the longitudinal Young's modulus as a function of the preludial compressive/tensile strain is next determined. The upgraded material model is then used in the present finite-element analysis.

Problem formulation

The problem analyzed in the present work involves finite-element modeling and analysis of a (simplified) plain-weaving process. The objective of the analysis is to assess

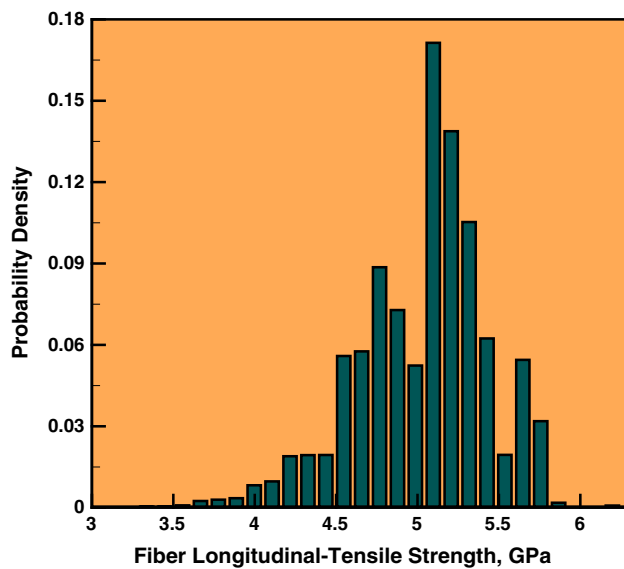


Fig. 9 Longitudinal-tensile strength probability density function of the defective as-synthesized PPTA fibers

the extent of damage sustained by, and the degree of longitudinal-tensile strength loss in, warp and weft PPTA yarns used in this process to manufacture single-ply fabrics.

Modeling and computational analysis

The finite-element computational approach employed in the present work requires specification of the following: (a) geometrical model; (b) meshed model; (c) computational algorithm; (d) initial conditions; (e) boundary conditions; (f) steps of analysis; (g) contact interactions; (h) material model(s); and (i) computational tool. These aspects are briefly overviewed in the remainder of this subsection.

Geometrical model

Two views of an example of the geometrical model/computational domain for the problem analyzed in this portion of the work are depicted in Fig. 11a–b. It is seen that the geometrical model includes five warp and five weft yarns. In the geometrical model shown in these figures, only two weft yarns (labeled 1 and 2) are present in the computational domain and have been engaged by the five warp yarns. In other words, the warp yarns are snaked about the (pre-tensioned) weft yarns 1 and 2, and tensioned at $\pm 45^\circ$ from the fabric plane to create a shed for the third weft yarn. The remaining three weft yarns are added to the model (one at a time) after each plain-weaving cycle. It should be noted that an oval cross-sectional area of the

yarns was adopted, in the present work, which is in accordance with the commonly observed yarn cross-sections in the plain-woven fabric, e.g., [31–34].

Meshed model

A close-up of the typical meshed model used in the present work is depicted in Fig. 12. Each warp and weft yarn is meshed using 88560 and 62315 three-dimensional continuum eight-node finite elements of comparable size, respectively. The mesh size used in the modeling of the plain-weaving process was determined by carrying out a mesh-sensitivity analysis and represents a compromise between the computational efficiency and accuracy.

Computational algorithm

All the calculations carried out in this portion of the work are based on a transient, displacement-based, purely Lagrangian, conditionally stable, explicit finite-element algorithm. Since the plain-weaving process is generally not associated with significant thermal effects, such effects are neglected in the present work and, consequently, only an isothermal (ambient temperature), purely mechanical analysis is carried out.

Initial conditions

At the beginning of the analysis, all the components of the computational model are assumed to be stationary and stress free.

Boundary conditions

The following boundary conditions were applied to the computational domain:

- Weft yarns*—each weft yarn present in the model during a given plain-weaving cycle is subjected to the predetermined axial tension. The magnitude of this tension is set to a prototypical value of 100 MPa [35]; and
- Warp yarns*—the end face of each warp yarn preceding the first weft yarn is kept fixed, while the opposite end faces are subjected to the axial tension of 100 MPa.

Steps of analysis

The total analysis is divided into a number of discrete steps, each corresponding to a single plain-weaving cycle. Within each of these analysis steps/cycles, the following is carried out:

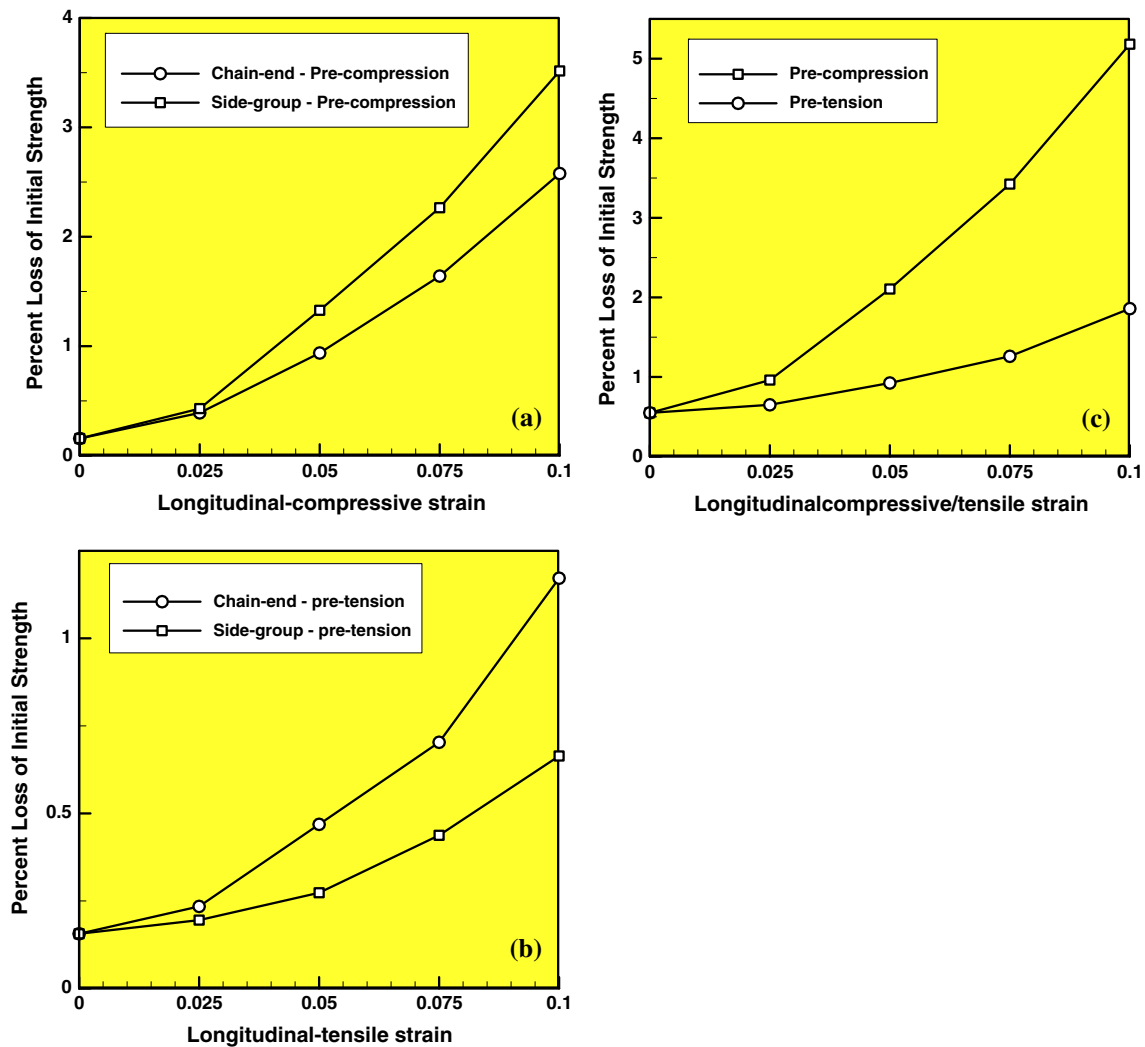


Fig. 10 Percent loss of mean fiber longitudinal-tensile strength, as a function of the magnitude of the preludial longitudinal: **a** compressive; and **b** tensile strain; and **c** master curve relating the extent of PPTA

- (i) at the beginning of each step, a new weft-yarn is added to the model and pre-tensioned;
- (ii) the two families of warp yarns (inclined at $+45^\circ$ and -45°) are advanced in the plane parallel to the plane of the fabric, by one weft-yarn spacing; and
- (iii) the two warp-yarn families are then swung in order to change the sign of their inclination angle. This was accomplished by moving the top two-pulley + belt mechanism downward and the bottom two-pulley + belt mechanism upward.

As seen in Fig. 13, couplings are attached to the ends of (each) warp yarn. The reference node of Coupling 1 has all degrees of freedom fixed, except for rotation about the y-axis (the axis collinear with the weft yarns). The reference node of Coupling 2, on the other hand, has two additional degrees

fiber/yarn longitudinal-tensile strength loss as a function of the preludial compressive/tensile longitudinal strain

of freedom (x - and z -translations) free. Belts 1 and 2 are connected to the reference node of Coupling 2. As seen in Fig. 13, pulling to the right downward on the free end of Belt 1 swings the respective family of warp yarns upward, while pulling to the right downward on the free end of Belt 2 swings the other family of warp yarns downward. Between consecutive pulling on the two belts, a new weft yarn is added (and incorporated into the woven fabric).

Contact interactions

Warp-yarn/weft-yarn interactions are all modeled using the penalty-type contact algorithm. Within this algorithm, (normal) penetration of the contacting surfaces is resisted by a set of linear springs which produce a contact pressure that is proportional to the depth of penetration. Typically,

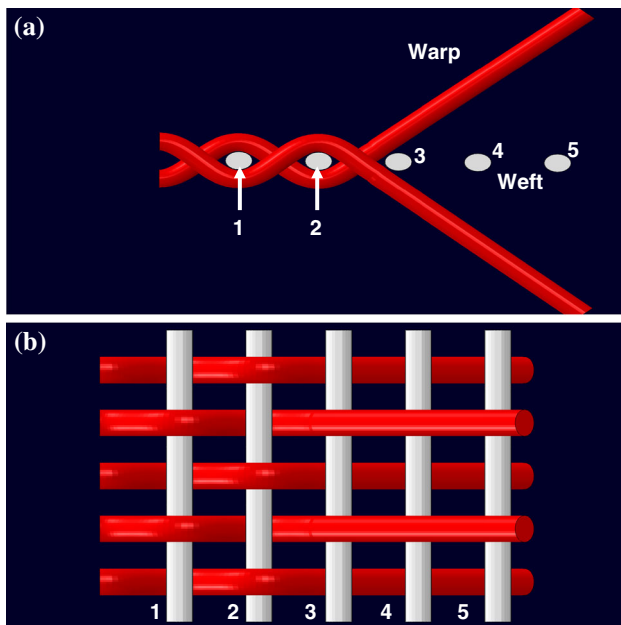


Fig. 11 **a** Side view; and **b** top view of an example of the geometrical model/computational domain for the finite-element analysis of the plain-weaving process

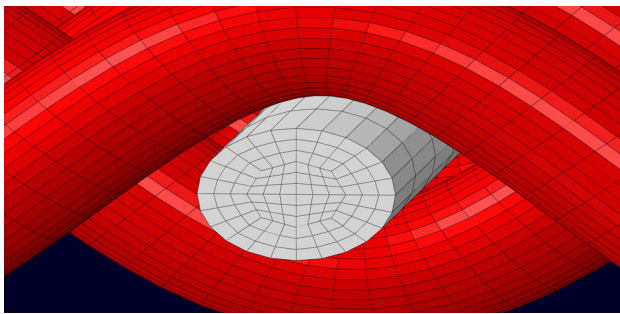


Fig. 12 A close-up of the typical meshed model used in the finite-element analysis of the plain-weaving process

maximum default values, which still ensure computational stability, are assigned to the (penalty) spring constants. Force equilibrium in a direction collinear with the contact interface normal then causes the penetration to acquire an equilibrium (contact pressure dependent) value. It should be noted that no contact pressures are developed unless (and until) the nodes on the “slave surface” contact/penetrate the “master surface.” On the other hand, the magnitude of the contact pressure that can be developed is unlimited. As far as the tangential contact interactions (responsible for transmission of the shear stresses across the contact interface) are concerned, they are modeled using a modified Coulomb friction law. Within this law, the maximum value of the shear stresses that can be transmitted (before the contacting surfaces begin to slide) is

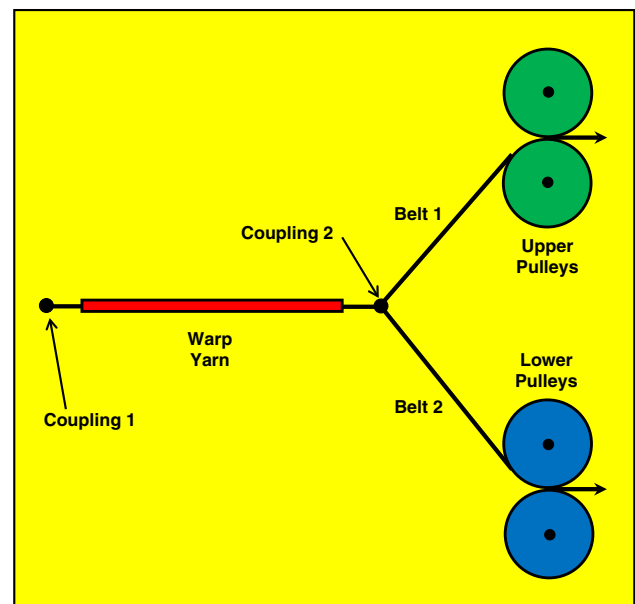


Fig. 13 The procedure used to carry out plain-weaving of the fabric. Please see text for details

defined by a product of the contact pressure and a static (before sliding) and a kinetic (during sliding) friction coefficient. In addition, to account for the potential occurrence of a “sticking condition” (sliding occurs by shear fracture of the softer of the two materials, rather than by a relative motion at the contact interface), a maximum value of shear stress (equal to the shear strength of the softer material) that can be transmitted at any level of the contact pressure is also specified [36]. It should be noted that, in order to account for the presence of yarn coating (not modeled explicitly), a low value of the friction coefficient $\mu = 0.05$ was used [8]. It should be also noted that within the yarns, friction may develop between the (lightly twisted) contacting fibers. Since the presence of discrete fibers within individual yarns is not modeled explicitly, this effect was accounted for during the formulation of the yarn-level material constitutive model. This was accomplished through the use of the so-called Digital Element Method and a pulled-fiber test [8].

Material models

As mentioned earlier, the same material model is used for the warp- and weft-yarns. The model was previously developed in Refs. [28–30] and upgraded using the coarse-grained molecular-level computational results presented in the previous section. The material constitutive model is of a linear orthotropic elastic character with progressively degradable longitudinal-tensile strength. The coarse-grained

molecular-level computational results are used to enrich this material model by making the degradation of the material tensile strength and Young's modulus be a function of the magnitude and the character (tension, compression, shear) of the prior and ongoing loading. This ensures that highly bent warp yarns at their compressive side undergo substantial strength/stiffness degradation which will prevent the development of unrealistically high local stresses. Since the failure tensile strain is assumed to be damage invariant, the material longitudinal Young's modulus is also treated as a progressively degradable material property.

Computational tool

The problem of plain-weaving process modeling is analyzed using an explicit solution algorithm implemented in ABAQUS/Explicit, a general-purpose finite-element solver [37]. This algorithm was chosen because it is associated with comparatively low computational cost when dealing with three-dimensional problems dominated by the contact interactions and model-change (i.e., progressive addition of the weft yarns). Since the dynamic, explicit finite-element formulation is only conditionally stable, care had to be taken to ensure that the time increments during the analysis do not exceed the critical time increment [38].

Results

The results presented in this subsection are used to help establish the effect of differences in the kinematics and deformation sustained by the warp and weft yarns during plain-weaving on their residual tensile strength.

Material distribution during plain-weaving

Material distribution in the course of four consecutive cycles of the plain-weaving process is shown in Fig. 14a–d. For clarity, weft yarns are colored white, while warp yarns are colored red in these figures. In Fig. 14a, it is seen that the first weft yarn (labeled 1) is completely engaged, while the second (labeled 2) has begun to be engaged by the vertically moving two families of warp yarns. At the identical instant during the subsequent plain-weaving cycle, Fig. 14b, it is seen that weft yarn 2 is completely engaged, while weft yarn 3 has begun to be engaged by the vertically moving two families of warp yarns. Figures 14c–d show, respectively, material distribution at the identical instants during the subsequent two weaving cycles. Examination of Fig. 14a–d reveals that each weaving cycle adds to the growing fabric section of a length equal to the weft-yarn spacing. It should be noted that, for improved clarity, the results presented in Fig. 14a–d are generated

under relatively low tensile loads applied to the warp and weft yarns. Consequently, relatively little distortion in the yarn cross-sectional area, except in the warp-yarn/weft-yarn contact region, is seen in these figures. The extent of yarn cross-section distortions increases with the magnitude of the tension forces applied to the warp and weft yarns.

Weaving-induced warp-/weft-yarn longitudinal-tensile strength loss

Since the warp and the weft yarns are subjected to bending and contact stresses/strains during plain-weaving, they experience structural damage and, in turn, a loss in the longitudinal-tensile strength. It should be noted that, in the present work, only the normal contact stresses/strains are assumed to give rise to the longitudinal-tensile strength loss. In other words, the effect of tangential contact stresses/strains is ignored. This was done for two reasons: (a) to account for the fact that fibers/yarns are generally coated to minimize the friction coefficient and, thus, sliding contact stresses/strains and (b) to recognize the fact that the coarse-grained analysis carried out in the present work strictly modeled only the interior portion of the PPTA fibers. The upgraded material model for the PPTA yarns, described earlier, treats the material longitudinal-tensile strength as a state variable, the evolution of which is governed by the loading history of the yarn. The loading history of the warp and weft yarns, in the present case, is associated with yarn crimping and contact accompanying plain-weaving. Distributions of the local loss (in GPa) in the longitudinal-tensile strength over a planar section (passing through the yarn neutral axis and orthogonal to the fabric mid-plane) of one of the warp and weft yarns are shown in Fig. 15a–b, respectively. It should be noted that the yarns depicted in these figures reside in the fabric produced by the plain-weaving process simulated in the present work. Examination of the results displayed in Fig. 15a–b clearly reveals that the warp yarns experience a larger extent of the longitudinal-tensile strength loss and the size of the compromised region is larger. Specifically, in the case of the warp yarns, the longitudinal-tensile strength loss could be as high as 0.28 GPa, while in the case of the weft yarns this loss is merely 0.08 GPa. Furthermore, in both types of yarns, the maximum loss in the longitudinal-tensile strength is observed in the yarn regions subjected to compression during plain-weaving.

Weaving-induced warp-/weft-yarn longitudinal-breaking strength reduction

In the previous section, it was demonstrated that the warp yarns and, to a lesser extent the weft yarns, experience a loss in their local longitudinal-tensile strength (modeled as

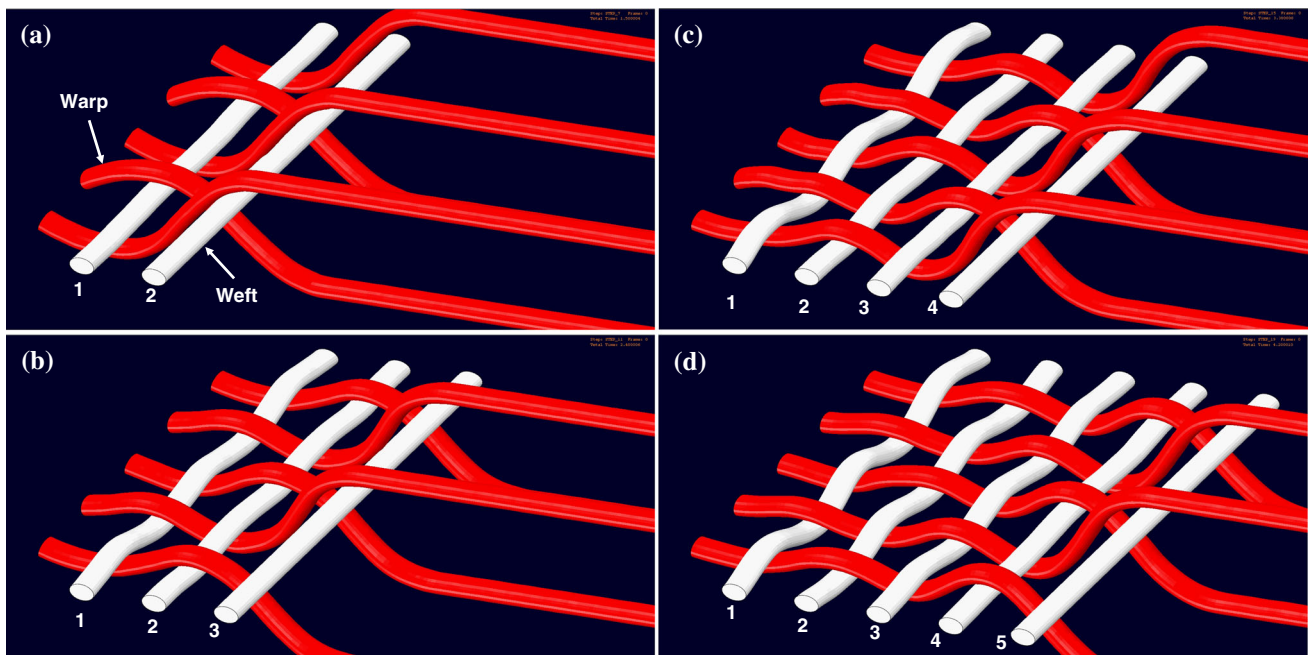


Fig. 14 Material distribution in the course of four consecutive cycles of the plain-weaving process

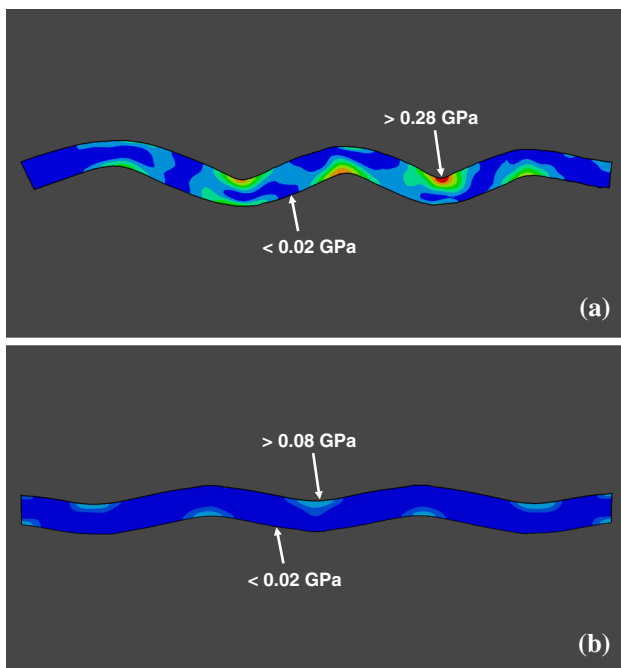


Fig. 15 Distributions of the local loss in the longitudinal-tensile strength over a planar section (passing through the yarn neutral axis and orthogonal to the fabric mid-plane) of one of the **a** warp; and **b** weft yarns residing in the plain-woven fabric

a material internal state variable) during plain-weaving. In this section, the yarns depicted in Fig. 15a–b are extracted from the fabric and subjected to axial loading (within a computational/virtual uniaxial-tensile test) until failure. This was accomplished by employing the same type of

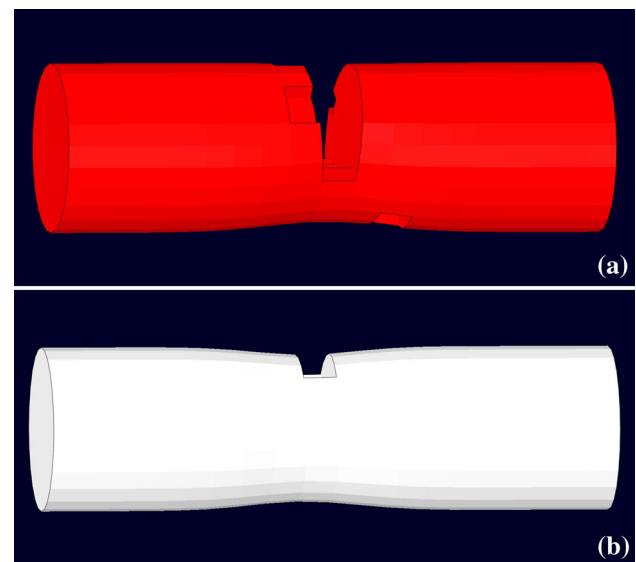


Fig. 16 The extent of failed-element deletion prior to yarn failure in the case of the: **a** warp; and **b** weft yarns extracted from the plain-woven fabric and subjected to uniaxial tension

finite-element analysis as the one used in the simulation of the plain-weaving process. Specifically, couplings are applied to the ends of the extracted yarns, and tensile forces are applied along the expected (straight) axis of the yarns. To assess the loss in the longitudinal-breaking strength induced by weaving, the same virtual uniaxial-tensile testing is applied to the as-synthesized PPTA yarns [39–42]. The results obtained show that the weaving-induced loss in the longitudinal-breaking strength is as follows: (a) warp

yarns—10–15 % and (b) weft yarns—0–5 %. These results are in reasonable agreement with their experimental counterparts reported in Ref. [14] as (a) warp yarns—10–25 % and (b) weft yarns—0–5 %. It should be noted that larger losses in the longitudinal-breaking strength than in the local longitudinal-tensile strength are observed in the present work. This is particularly true in the case of the warp yarns. The reason for this is that the finite elements within the yarn with the most compromised longitudinal-tensile strength become deleted in the early stages of the virtual uniaxial testing. Deletion of these elements creates local stress-concentration effects, leading to premature failure. This is demonstrated in Fig. 16a–b, in which the extent of failed-element deletion prior to yarn failure is clearly greater in the warp-yarn case, Fig. 16a, than in the weft-yarn case, Fig. 16b. It should be further noted that, for improved clarity, only short segments (containing the region of ultimate failure) of the two yarns are displayed in Fig. 16a–b.

Conclusions

Based on the results obtained in the present work, the following summary remarks and main conclusions can be drawn:

1. The problem of plain-weaving-induced damage and the associated loss in the longitudinal-tensile strength of the warp and weft yarns of PPTA is investigated computationally.
2. Two computational modeling/simulation techniques are employed: (a) coarse-grained molecular-level analysis is first carried out to assess the effect of preludial axial - compressive/tensile (bending) loading on the longitudinal-tensile strength of the PPTA yarns and (b) then a conventional displacement-based finite-element analysis of the plain-weaving process is conducted in order to assess the extent of longitudinal-tensile strength of the PPTA warp and weft yarns under common plain-weaving fabric-manufacturing conditions.
3. The results obtained clearly revealed that warp yarns, due to their more extensive crimping, sustain more damage during the plain-weaving process and, hence, possess an inferior longitudinal-tensile strength.
4. The computed results are compared with the available public-domain experimental data and a reasonable experiment-to-computation agreement is found.

Acknowledgements The material presented in this paper is based on work supported by three Army Research Office sponsored grants entitled “*Multi-length Scale Material Model Development for Armor-grade Composites*” (Contract Number W911NF-09-1-0513), “*Friction Stir Welding Behavior of Selected 2000-series and*

5000-series Aluminum Alloys” (Contract Number W911NF-11-1-0207), and “*Concept Validation and Optimization for a Vent-based Mine-blast Mitigation System*” (Contract Number W911NF-11-1-0518). The authors are indebted to Dr. Ralph A. Anthenien, Jr., and Dr. Bryan J. Glaz of ARO for their continuing support and interest in the present work.

References

1. Grujicic M, Yavari R, Snipes JS, Ramaswami S, Runt J, Tarter J, Dillon G (2012) Molecular-level computational investigation of shock-wave mitigation capability of polyurea. *J Mater Sci* 47:8197–8215. doi:10.1007/s10853-012-6716-4
2. Edmunds R, Wade MA (2005) On kink banding in individual PPTA fibres. *Compos Sci Technol* 65:1284–1298
3. Dobb MG, Johnson DJ, Saville BP (1981) Compressional Behaviour of Kevlar Fibres. *Polymer* 22:960–965
4. Kwolek SL (1972) Optically anisotropic aromatic polyamide dopes, U.S. Patent 3,671,542
5. du Pont EI (1983) Technical brochure, Weight Savings for Aircraft using Kevlar Aramid Fiber
6. Blades H (1973) Dry jet wet spinning process, U.S. Patent 3,767,756
7. Grujicic M, Bell WC, Glomski PS, Pandurangan B, Yen C-F, Cheeseman BA (2011) Filament-level modeling of aramid-based high performance structural materials. *J Mater Eng Perform* 20:1401–1413
8. Grujicic M, Bell WC, Glomski PS, Pandurangan B, Yen C-F, Cheeseman BA (2011) Multi-length scale computational derivation of Kevlar[®] yarn-level material model. *J Mater Sci* 46:4787–4802. doi:10.1007/s10853-011-5389-8
9. Grujicic M, Pandurangan B, Snipes JS, Yen C-F, Cheeseman BA (2013) Multi-length scale enriched continuum-level material model for Kevlar[®]-fiber reinforced polymer–matrix composites. *J Mater Eng Perform* 22:681–695
10. Grujicic M, Ramaswami S, Snipes JS, Yavari R, Lickfield G, Yen C-F, Cheeseman B (2013) Molecular-level computational investigation of mechanical transverse behavior of *p*-phenylene terephthalamide (PPTA) fibers. *Multidiscip Model Mater Struct* 9:462–498
11. Grujicic M, Yavari R, Snipes JS, Ramaswami S, Yen C-F, Cheeseman BA (2013) Molecular-level study of the effect of prior axial compression/torsion on the axial-tensile strength of PPTA fibers. *J Mater Eng Perform* 22:3269–3287
12. Grujicic M, Ramaswami S, Snipes JS, Yavari R, Yen C-F, Cheeseman BA (2013) Axial-compressive behavior, including kink-band formation and propagation, of single *p*-phenylene terephthalamide (PPTA) fibers. *Adv Mater Sci Eng* 2013, Article ID 329549
13. Lim JS, Lee BH, Lee CB, Han I-S (2012) Effect of the weaving density of aramid fabrics on their resistance to ballistic impacts. *Engineering* 4:944–949
14. Sanborn B, Racine N, Weerasooriya T (2012) The effect of weaving on the strength of Kevlar KM2 single fibers at different loading rates. ARL-TR-6280, US Army Research Laboratory
15. Rocher J-E, Allaoui S, Hivet G, Blond E (2012) Experimental characterization of the tensile behavior of a polypropylene/glass 3D-fabric: from the yarn to the fabric. In: 4th world conference on 3D fabrics and their applications, Aachen
16. Hunt W, Abu Obaid A, Burleigh A Curvature induced kink bands and the resulting degradation of the tensile properties of synthetic fiber. Poster presented at the 35th anniversary of the Center for Composite Materials, University of Delaware

17. Burleigh A, Hunt W, Abu-Obaid A Effects of 2D and 3D-weaving process on tensile properties of synthetic fibers. Poster presented at the 35th anniversary of the Center for Composite Materials, University of Delaware
18. <http://accelrys.com/products/datasheets/materials-visualizer.pdf>. Accessed 7 April 2014
19. Grujicic M, Sun Y-P, Koudela KL (2007) The effect of covalent functionalization of carbon nanotube reinforcements on the atomic-level mechanical properties of poly-vinyl-ester-epoxy. *Appl Surf Sci* 253:3009–3021
20. Grujicic M, Bell WC, Biggers SB, Koudela KL, Cheeseman BA (2008) Enhancement of the ballistic-protection performance of E-glass reinforced poly-vinyl-ester-epoxy composite armor via the use of a carbon-nanotube forest-mat strike face. *J Mater Des Appl* 222:15–28
21. Grujicic M, Pandurangan B, King AE, Runt J, Tarter J, Dillon G (2011) Multi-length scale modeling and analysis of microstructure evolution and mechanical properties in polyurea. *J Mater Sci* 46:1767–1779. doi:10.1007/s10853-010-4998-y
22. Grujicic M, Snipes JS, Ramaswami S, Yavari R, Runt J, Tarter J, Dillon G (2013) Coarse-grained molecular-level analysis of polyurea properties and shock-mitigation potential. *J Mater Eng Perform* 22:1964–1981
23. Grujicic M, Snipes JS, Ramaswami S, Yavari R, Ramasubramanian MK (2014) Meso-scale computational investigation of shock-wave attenuation by trailing release-wave in different grades of polyurea. *J Mater Eng Perform* 23:49–64
24. <http://accelrys.com/products/datasheets/discover.pdf>. Accessed 7 April 2014
25. Newell JA, Sagendorf MT (1999) Experimental verification of the end-effect weibull model as a predictor of the tensile strength of Kevlar 29 (poly *p*-phenylene terephthalamide) at different gage lengths. *High Perform Polym* 11:297–305
26. Steenbakkers LW, Wagner HD (1988) Elasticity and mechanical breakdown of Kevlar 149 aramid fibers by probabilistic approach. *J Mater Sci Lett* 7:1209–1212
27. Knoff WF (1987) A modified weakest-link model for describing strength variability of Kevlar aramid fibers. *J Mater Sci* 22:1024–1030. doi:10.1007/BF01103546
28. Grujicic M, Hariharan A, Pandurangan B, Yen C-F, Cheeseman BA, Wang Y, Miao Y, Zheng JQ (2012) Fiber-level modeling of dynamic strength of Kevlar® KM2 ballistic fabric. *J Mater Eng Perform* 21:1107–1119
29. Grujicic M, Pandurangan B, Bell WC, Yen C-F, Cheeseman BA (2011) Application of a dynamic-mixture shock-wave model to the metal–matrix composite materials. *Mater Sci Eng A* 528:8187–8197
30. Grujicic M, Bell WC, Pandurangan B, Yen C-F, Cheeseman BA (2011) Computational investigation of structured shocks in Al/SiC-particulates metal matrix composites. *Multidiscip Model Mater Struct* 7:469–497
31. Grujicic M, Arakere G, He T, Gogulapati M, Cheeseman BA (2008) A numerical investigation of the influence of yarn-level finite-element model on energy absorption by a flexible-fabric armor during ballistic impact. *J Mater Des Appl* 222:259–276
32. Grujicic M, Bell WC, Arakere G, He T, Cheeseman BA (2009) A meso-scale unit-cell based material model for the single-ply flexible-fabric armor. *Mater Des* 30:3690–3704
33. Grujicic M, Bell WC, He T, Cheeseman BA (2008) Development and verification of a meso-scale based dynamic material model for plain-woven single-ply ballistic fabric. *J Mater Sci* 43:6301–6323. doi:10.1007/s10853-008-2893-6
34. Grujicic M, Bell WC, Arakere G, He T, Xie X, Cheeseman BA (2010) Development of a meso-scale material model for ballistic fabric and its use in flexible-armor protection systems. *J Mater Eng Perform* 19(1):22–39
35. Miao Y, Zhou E, Wang Y, Cheeseman BA (2008) Mechanics of textile composites: micro-geometry. *Compos Sci Technol* 68:1671–1678
36. Grujicic M, Pandurangan B, d'Entremont BP, Yen C-F, Cheeseman BA (2012) The role of adhesive in the ballistic/structural performance of ceramic/polymer–matrix composite hybrid armor. *Mater Des* 41:380–393
37. ABAQUS version 6.10EF, user documentation, Dassault Systèmes, 2011
38. Grujicic M, Pandurangan B, Zecevic U, Koudela KL, Cheeseman BA (2007) Ballistic performance of alumina/S-2 glass-reinforced polymer–matrix composite hybrid lightweight armor against armor piercing (AP) and non-AP projectiles. *Multidiscip Model Mater Struct* 3:287–312
39. Grujicic M, d'Entremont BP, Pandurangan B, Runt J, Tarter J, Dillon G (2012) Concept-level analysis and design of polyurea for enhanced blast-mitigation performance. *J Mater Eng Perform* 21:2024–2037
40. Grujicic M, He T, Pandurangan B (2011) Development and parameterization of an equilibrium material model for segmented polyurea. *Multidiscip Model Mater Struct* 7:96–114
41. Grujicic M, Chittajallu KM, Cao G, Roy WN (2005) An atomic level analysis of conductivity and strength in poly (ethylene oxide) sulfonic acid based solid polymer electrolytes. *Mater Sci Eng B* 117:187–197
42. Grujicic M, Chittajallu KM, Walsh S (2003) Optimization of the VARTM process for enhancement of the degree of devolatilization of polymerization by-products and solvents. *J Mater Sci* 38:3729–3739